

RESEARCH ARTICLE

10.1002/2015JD023283

Key Points:

- Lagrangian dust transport model applied to new field data from the Sahara
- Dust emission is underestimated due to parameterized moist convection
- Airborne in situ and remote dust data constrain emission in sensitivity tests

Supporting Information:

- Movie S1
- Figure S1

Correspondence to:

H. Sodemann,
harald.sodemann@uib.no

Citation:

Sodemann, H., T. M. Lai, F. Marengo, C. L. Ryder, C. Flamant, P. Knippertz, P. Rosenberg, M. Bart, and J. B. McQuaid (2015), Lagrangian dust model simulations for a case of moist convective dust emission and transport in the western Sahara region during Fennec/LADUNEX, *J. Geophys. Res. Atmos.*, 120, 6117–6144, doi:10.1002/2015JD023283.

Received 2 MAR 2015

Accepted 19 MAY 2015

Accepted article online 29 MAY 2015

Published online 23 JUN 2015

Lagrangian dust model simulations for a case of moist convective dust emission and transport in the western Sahara region during Fennec/LADUNEX

H. Sodemann^{1,2}, T. M. Lai¹, F. Marengo³, C. L. Ryder⁴, C. Flamant⁵, P. Knippertz^{6,7}, P. Rosenberg⁷, M. Bart^{7,8}, and J. B. McQuaid⁷

¹Institute for Atmosphere and Climate, ETH Zürich, Zürich, Switzerland, ²Now at Geophysical Institute, University of Bergen, Bergen, Norway, ³Observational Based Research, Met Office, Exeter, UK, ⁴Department of Meteorology, University of Reading, Reading, UK, ⁵Sorbonne Universités, UPMC Université Paris 6, CNRS & UVSQ, UMR8190 LATMOS, Paris, France, ⁶School of Earth and Environment, University of Leeds, Leeds, UK, ⁷Now at Institute for Meteorology and Climate Research, Karlsruhe Institute of Technology, Karlsruhe, Germany, ⁸Aeroqual Ltd., Auckland, New Zealand

Abstract Due to the harshness and inaccessibility of desert regions, the uncertainties concerning the processes of dust mobilization at the surface, airborne transport, and sedimentation are still considerable, limiting the ability to perform model simulations. In June 2011, a comprehensive data set of ground-based and airborne in situ measurements and remote sensing observations was acquired within the Fennec/Lagrangian Dust Source Inversion Experiment (LADUNEX) field campaign in the western Sahara region. Here we evaluate the ability of the state-of-the-art Lagrangian particle dispersion model FLEXPART, newly fitted with a dust mobilization capability, to simulate dust transport in this region. We investigate a case where a large mesoscale convective system (MCS) triggered dust emissions in central Mali, which subsequently moved as a large cold pool dust front toward northern Mauritania. Specifying dust mobilization for this case is shown to be an important obstacle to simulating dust transport during this event, since neither the MCS nor the associated cold pool-causing dust emission is represented in the meteorological analysis. Obtaining a realistic dust transport simulation for this case therefore requires an inversion approach using a manual specification of the dust sources supported by satellite imagery. When compared to in situ and remote sensing data from two aircraft, the Lagrangian dust transport simulations represent the overall shape and evolution of the dust plume well. While accumulation and coarse mode dust are well represented in the simulation, giant mode particles are considerably underestimated. Our results re-emphasize that dust emission associated with deep moist convection remains a key issue for reliable dust model simulations in northern Africa.

1. Introduction

In many regions of the world, desert dust, or mineral aerosol, influences weather and climate through radiative and cloud feedbacks. The Sahara desert is the largest global dust source [Goudie and Middleton, 2001]. Dust mobilized here plays a role for local coupling to the West African summer monsoon [Parker *et al.*, 2005a, 2005b; Messenger *et al.*, 2009] but also influences the larger-scale region, for example, by providing cloud condensation nuclei to Europe [Klein *et al.*, 2010], by providing the (disputed) potential to influence hurricane activity in the tropical Atlantic [Dunion and Velden, 2004; Braun *et al.*, 2013], and by delivering nutrients to the Caribbean and the Amazon forest [Prospero and Lamb, 2003; Duce *et al.*, 1991].

Regarding the whole life cycle of Saharan mineral aerosol, including mobilization in the source regions, upward mixing in the convective boundary layer (CBL), long-range transport in the Saharan Air Layer [Cuesta *et al.*, 2009], and finally wet or dry deposition, the first and last aspects are among the most uncertain [Knippertz and Todd, 2012; Huneeus *et al.*, 2011]. Evan *et al.* [2014] found that all Coupled Model Intercomparison Project Phase 5 (CMIP5) models are unable to accurately replicate both emission and transport of dust. The simulated atmospheric dust burden above the largest global source region is therefore subject to substantial uncertainty. A number of field campaigns have been carried out in recent years around the Sahara region to better understand dust-related phenomena in this climatologically and logistically harsh environment. The African Monsoon Multidisciplinary Analysis (AMMA) program, among other important aspects, targeted the impact of aerosol particles on weather and climate in the Sahel region [Redelsperger *et al.*, 2006].

Marticorena et al. [2010] provide a multiyear climatology of dust export and deposition along a longitudinal transect in the Sahel. The Saharan Mineral Dust Experiment (SAMUM 1 and 2) project specifically focused on the optical properties and other physical and chemical characteristics of the mineral aerosol in the western Sahara region [*Heintzenberg, 2009; Ansmann et al., 2011*], as did the Dust and Biomass Burning Experiment (DABEX) [*Haywood et al., 2008*] and Dust Outflow and Deposition to the Ocean (DODO) projects [*McConnell et al., 2008*]. Notably, though, none of the previous research efforts so far explicitly focused on the Saharan Heat Low region [*Todd et al., 2013*].

The purpose of the British-French Fennec field program was to study the conditions leading to dust mobilization and transport in parts of Mauritania, Mali, and Algeria in order to improve the understanding of and to quantify physical processes controlling the Saharan climate system [*Ryder et al., 2015*]. Particular emphasis was on using models and observations synergistically in order to evaluate weather and climate models for that region [*Washington et al., 2012*]. In the first Fennec field campaign, which took place in the western and central Sahara during June 2011, dust mobilization and transport were investigated with state-of-the-art measurement equipment in a large international effort involving two aircraft and an extensive network of ground-based measurements [*Todd et al., 2013; Marsham et al., 2013; Hobby et al., 2013; Ryder et al., 2015*]. The Lagrangian Dust Source Inversion Experiment (LADUNEX) embedded within the Fennec program was dedicated to obtaining an airborne reference data set which, for a substantial mobilization event, would make it possible to reproduce the measured atmospheric dust burden by a Lagrangian transport model. One aim thereby is to single out the importance of atmospheric dust transport and mobilization on atmospheric dust concentrations, allowing us to validate dust simulations based on operational weather analyses. For the Fennec super site station Bordj Badji Mokhtar in southern Algeria, it was shown that dust storms resulting from convective cold pool formation, so-called haboobs, are the most important dust mobilization mechanism in the region, followed by downward mixing of momentum from low-level jets [*Marsham et al., 2013; Allen et al., 2013*]. This confirmed an earlier hypothesis by *Marsham et al.* [2008], at least for the summer field season of the Fennec campaign in June 2011. Such haboobs can travel over hundreds of kilometers across the Sahara, with a dust front elevating up to 3 km in the vertical and a horizontal extent of several hundred kilometers [*Flamant et al., 2007; Knippertz et al., 2007*]. The mesoscale dimensions of these features, and the fact that they can be generated in relation to synoptic-scale monsoon surges [e.g., *Flamant et al., 2007; Bou Karam et al., 2008*], allow simulation of the dust mobilization and transport related to haboobs in a suitable model setup. As *Weisman et al.* [1997] pointed out, cold pool dynamics can be sufficiently represented in models at grid scales of 12 km, their dynamics essentially being hydrostatic. The most critical component remains the parameterization of convection. Using 40 day convection-permitting simulations from summer 2006, *Marsham et al.* [2011] and *Heinold et al.* [2013] showed that haboobs are a dominant mechanism for dust mobilization (followed by low-level jets), yet they are essentially missing in models with parameterized moist convection. Mesoscale weather prediction model simulations at convection-permitting resolution in contrast are able to simulate long-lived, extensive cold pools with a realistic three-dimensional structure resulting from moist convection [*Knippertz et al., 2009; Kocha et al., 2013; Bou Karam et al., 2014; Roberts and Knippertz, 2014*].

The actual mobilization of dust grains at the ground by atmospheric processes takes place at scales not resolved by weather prediction and climate models and requires parameterization. This renders dust mobilization a challenging aspect of simulating the atmospheric dust burden. Dust mobilization is most often parameterized based on empirical findings or sometimes bypassed completely by including it as an aerosol climatology in atmospheric models [*Tompkins et al., 2005*]. Most commonly, dust emission has been described by a power law function where the dust emission is related to friction velocity near the surface [e.g., *Tegen and Fung, 1994; Shao et al., 1993*]. Additional constraints come from the grain size and erodibility of the soil material, vegetation cover, and soil moisture [*Marticorena and Bergametti, 1995; Tegen et al., 2002*]. While the third-order relation to friction velocity is well established, most of the additional uncertainty of, for example, the particle size distribution is combined in one uniform free scalar (uplift factor) that converts to units of a mass flux [*Tegen and Fung, 1994*]. Often, this uplift factor has to be determined a posteriori, which is difficult given the sparsity of available measurements. Also, the response of individual models to meteorological factors only cannot clearly be identified. *Marsham et al.* [2011] therefore proposed the so-called dust uplift potential as a means for model comparisons, allowing us to isolate the influence of

meteorology from soil and other properties. Recently, a much more complex approach to dust mobilization has been proposed by *Kok and Renno* [2009]. These authors suggest that dust mobilization can be parameterized based on first principles rather than empirical relations by considering dust as a so-called brittle material. This approach holds high promise for providing more realistic dust emission in future simulation experiments [*Kok*, 2011], as demonstrated recently for an Earth system model [*Albani et al.*, 2014].

Eulerian grid-scale models have commonly been used to simulate dust mobilization and transport [e.g., *Heinold et al.*, 2007]. Using nested grids up to horizontal grid spacings below 1 km, *Solomos et al.* [2012] were able to analyze the detailed structure of a density current in the Atlas Mountains. For models with large horizontal grid spacings, such as global weather prediction and climate models, it is difficult to retain the fine-scale structure of dust transport. Off-line Lagrangian transport modeling tools are in principle more capable of retaining fine-scale structures with the evolving atmospheric flow due to the absence of numerical diffusion, even when run with medium-resolution meteorological fields [*Sodemann et al.*, 2011; *Rastigejev et al.*, 2010]. This is particularly useful to study the evolution of small-scale features with large gradients, such as dust fronts using operational weather analysis or reanalysis data. Backward trajectories have therefore been used in a number of studies in the past to study the transport of mineral aerosol. *Sodemann et al.* [2006], for example, used additional objective criteria along backward trajectories to reconstruct the mobilization regions and transport paths for events of long-range dust transport. *Draxler et al.* [2001, 2010] extended the Hysplit model [*Draxler and Hess*, 1998] with a dust mobilization code.

In this study, we employ for the first time the widely used Lagrangian particle dispersion model Flexible Particle dispersion model (FLEXPART) [*Stohl et al.*, 2005] to simulate desert dust mobilization, transport, and deposition. In contrast to simple backward trajectories, quantitative comparisons between measurements and FLEXPART model simulations can be carried out due to the large number of particles representing aerosol mass. Aerosol transport simulated with FLEXPART has recently been shown to correspond well with airborne observations of volcanic ash [*Kristiansen et al.*, 2012]. A problem that will affect all modeling efforts in this region of the world similarly is the sparsity of the meteorological network for routine ground-based measurements.

In principle, Lagrangian models offer the possibility to invert atmospheric observations into emission functions using inverse methods [e.g., *Eckhardt et al.*, 2008; *Kristiansen et al.*, 2012]. The application of this powerful tool requires, however, substantial amounts of quantitative data to sufficiently modify the a priori fields. While the observational data obtained during the Fennec field program are still too sparse to sufficiently constrain an objective computational inversion method, manual inverse transport modeling can be used to constrain the region and magnitude of dust mobilization.

The purpose of this paper is threefold:

1. It aims to present the field observations during the LADUNEX flight on 20 June 2011. During this flight, the aircraft sampled within a cold pool triggered dust front generated by a large MCS one day after dust mobilization using in situ and remote sensing instrumentation, thereby providing a data set to quantitatively validate model simulations.
2. It aims to demonstrate the main factors of uncertainty when simulating dust mobilization and dust transport for the above case during the Fennec campaign. Hereby, the main goal is to separate the respective roles of different meteorological factors for the failure or success of the simulation, and to outline the potential for future improved parameterizations for dust mobilization due to haboobs in grid-scale models.
3. It aims to outline the potential of inverse transport modeling for estimating dust emission sources and strengths from comparison between model simulations and airborne measurements.

In the following, we present the field data used for this study, as well as the modeling tools and setups used to simulate dust emission and transport. Section 3 describes dust transport as observed from in situ and remote sensing observations for the case analyzed here. Section 4 presents experiments with the Lagrangian model, which allow us to reproduce the observed dust transport pattern using an effective dust source. Simulation results for the “best match” simulation are compared in detail to field observations in section 5. Section 6 investigates the potential causes for the difficulties to model dust mobilization and transport for this case, before conclusions are presented in section 7.

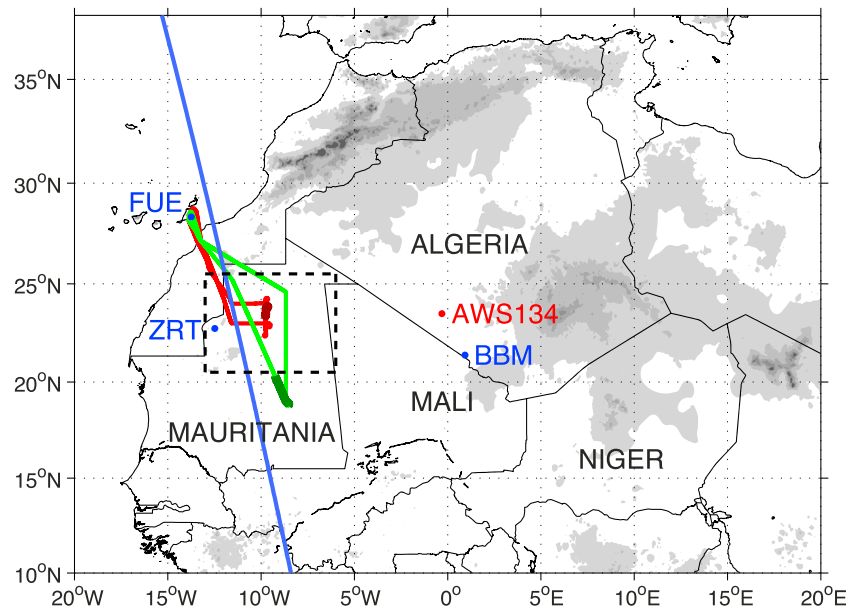


Figure 1. Study area, including Fennec supersite 1 at Bordj Badji Mokhtar (BBM), supersite 2 at Zouerate (ZRT), aircraft base Fuerteventura (FUE), automatic weather station 134 (AWS134), flight tracks of the BAe-146 (red) and Falcon 20 (green), and CALIOP satellite overpass (blue) during 20 June 2011. Orography above 500 m is shaded. Dashed black box denotes zoom area shown in Figure 4.

2. Data and Methods

2.1. Field Observations During Fennec/LADUNEX

The Fennec field program provided comprehensive observational data on the meteorological conditions leading to dust mobilization and transport in the otherwise data-sparse region of Mali and Mauritania. A large number of ground-based measurements were made from automated weather stations (AWS) [see *Hobby et al.*, 2013] and two manned and heavily instrumented “super sites” [Marshall *et al.*, 2013; Todd *et al.*, 2013], one of which was located at Bordj Badji Mokhtar (BBM) in southern Algeria (21.38°N, 0.92°E, 420 m above mean sea level (msl)) (see Figure 1). Here we use data from AWS134 (23.50°N, 0.30°W, 324 m msl), located near BBM, which recorded 2 m temperature, humidity, and wind speed and direction, as well as pressure at a 200 s time interval.

In addition, two research aircraft were deployed during Fennec 2011, operating from Fuerteventura, Canary Islands, Spain. Instrumentation onboard the UK’s BAe-146-301 research aircraft operated by the Facility for Airborne Atmospheric Measurements (FAAM) used here includes a Vaisala AVAPS dropsonde system, a three-wavelength nephelometer measuring at 1 Hz, a LEOSPHERE ALS450 aerosol lidar [Marenco *et al.*, 2011], and a suite of instruments measuring particle size. The latter provides size-resolved measurements between 0.1 and 300 μm averaged over 5 min intervals for horizontal runs or over 200 m for vertical profiles [Ryder *et al.*, 2013a, 2013b]. These particle size data have been corrected based on Mie theory assuming spherical particles and an appropriate refractive index [Rosenberg *et al.*, 2012]. In situ extinction was derived from the sum of scattering (from the nephelometer) and absorption from the Particle Soot Absorption Photometer (PSAP) measurements. The nadir-viewing lidar provided backscatter and depolarization at 355 nm with a vertical resolution of 1.5 m and an integration time of 2 s. The signal-to-noise ratio for the dust-laden atmosphere in the measurement region, however, caused difficulties to invert the lidar signal into extinction. It was thus required to decrease the resolution to 300 m in the vertical and a 60 s integration time, translating into a ~ 9 km along-track footprint at a typical ground speed of $\sim 150 \text{ m s}^{-1}$. Aerosol extinction coefficients have been computed from the lidar signal using the method by Marenco [2013]. Note that, in below 1000–1500 m, the uncertainty in the extinction coefficient is of the order of 100% and of the order of 10–20% above 2000 m. The lidar also has depolarization capability, which is however used qualitatively only because of an uncharacterized channel crosstalk, and in this paper, no absolute estimation of depolarization is attempted.

The SAFIRE (Service des Avions Français Instrumentés pour la Recherche en Environnement) Falcon 20 operated the nadir-pointing backscatter lidar Leandre New Generation [LNG, *de Villiers et al.*, 2010], which measures atmospheric reflectivity of aerosols at three wavelengths (355, 532, and 1064 nm) below the aircraft from an altitude of 11 km msl. Furthermore, the aircraft was equipped with a Vaisala AVAPS dropsondes launching device and additional instrumentation as detailed by *Ryder et al.* [2015]. Profiles of the atmospheric extinction coefficient at 532 nm were retrieved using standard lidar inversion techniques [*Fernald et al.*, 1972; *Cuesta et al.*, 2008]. Profiles of the molecular extinction coefficient used in the inversion were derived from molecular density profiles computed using temperature and pressure from dropsondes released during the flight [*Bodhaine et al.*, 1999]. A constant aerosol backscatter-to-extinction ratio of 0.021 sr^{-1} was used for the inversion. A backscatter ratio (total backscatter coefficient divided by molecular backscatter coefficient) of 1 has been assumed at 9.5 km above ground level, that is, in generally dust-free conditions. The resolution of the data used here is 30 m in the vertical and 10 s integration time, translating into a horizontal resolution of 2 km at a typical ground speed of 200 m s^{-1} .

Here we focus on a particular period during June 2011 when a large mesoscale convective system (MCS) in northeastern Mali triggered dust mobilization in a cold pool between 0000 and 0830 UTC on 19 June 2011, which was then transported into the operational range of the aircraft stationed in Fuerteventura, Spain (FUE, Figure 1) during the following 48 h. The red line in Figure 1 depicts the track of flight b604 of the BAe-146 during 1247 to 1751 UTC on 20 June 2011. The BAe-146 probed the horizontal gradient and vertical structure at the southern boundary of a dusty air mass while releasing nine dropsondes. The green line shows the track of flight #21 of the Falcon 20 from 1322 to 1700 UTC on 20 June 2011. The Falcon 20 surveyed the larger area of the dust plume and across the intertropical discontinuity (ITD) with the lidar while releasing 11 dropsondes at 11 km msl. In addition, the CALIOP satellite passed over the area within the time of the flights (blue line). While beyond the scope of the current paper, a detailed comparison of aircraft data with the CALIOP retrievals, including the track segment denoted in blue in Figure 1, shows a general underestimation of aircraft AOD (*V. Pappas et al.*, Comparison of Fennec airborne in situ dust measurements with CALIOP spaceborne lidar retrievals of extinction, manuscript in preparation, 2015). Nonetheless, *Banks et al.* [2013] demonstrated that the airborne LIDAR observations during Fennec are consistent with AOD products from a number of satellite sensors.

2.2. Additional Data Products

The “dust RGB” product from EUMETSAT’s Meteosat Second Generation (MSG) Spinning Enhanced Visible and Infrared Imager (SEVIRI) provided qualitative information on atmospheric dust content at a 15 min time interval and at 3 km pixel size. This widely used qualitative remote sensing product indicates dust load in the atmospheric column above 1.5 km in sufficiently dry air (integrated water vapor (IWV) $< 25 \text{ mm}$) [*Brindley et al.*, 2012; *Banks et al.*, 2013].

For the present simulations, the European Centre for Medium-Range Weather Forecasts’ (ECMWF) global operational analysis data (natively run at a spectral resolution of T1279 and 91 hybrid levels in the vertical) interpolated to a horizontal grid spacing of $1^\circ \times 1^\circ$ were used, supplemented by a high-resolution nest of the same operational analysis data with a grid spacing of $0.25^\circ \times 0.25^\circ$ (corresponding to a grid spacing of $\sim 28 \text{ km}$ at the equator), covering a regional domain (20°W – 20°E ; 10°N – 35°N). The nesting at different resolutions provided a higher resolution of the meteorological variables in the region of main interest, while maintaining the overall computations feasible. Typically, about 25–30 layers represent the 5–6 km deep daytime Saharan boundary layer, and about 12 layers are within the lowest 1 km above the surface. The analysis data were supplemented by +3 h meteorological forecast data, providing a higher temporal resolution of the input data, as well as surface fluxes and precipitation. Three hourly accumulated precipitation from the operational forecasts was converted to hourly precipitation rates [*Stohl et al.*, 2005]. Hourly averaged output of the FLEXPART simulation in terms of three-dimensional atmospheric dust mass concentration for all size classes (see next section) was saved for a horizontal domain covering the region 20°W – 30°E , 0 – 40°N at a $0.25^\circ \times 0.25^\circ$ grid spacing, and 25 vertical levels at a $\sim 0.5 \text{ km}$ interval from the surface up to 13 km above ground. For the meteorological description of the study period and the corresponding Lagrangian particle transport model simulations (section 3), the same operational analyses of pressure, temperature, winds, and humidity were used.

2.3. Dust Transport Model Simulations

Dust transport was simulated by means of the Lagrangian Particle Dispersion model FLEXPART [Stohl *et al.*, 2005]. The FLEXPART model simulates aerosol transport in hypothetical air parcels using three-dimensional wind fields, while taking into account settling and wet and dry deposition processes. Dust is injected into the model atmosphere by an off-line preprocessor (named DustBowl) and represented by air parcels containing a certain dust mass for a given size class (described in more detail below). After injection, dust transport and deposition are simulated online by the FLEXPART model. Large-scale advection is calculated from grid-scale wind velocities. An internal time step of 900 s is applied here, and a linear interpolation between the 3-hourly meteorological data. Turbulent dispersion in the boundary layer, including dry convection, is parameterized using the Langevin equations, taking into account the predominant stability regime in the boundary layer [Thomson, 1987]. Vertical redistribution due to moist convection is parameterized based on the mass flux parameterization scheme of Emanuel and Živković-Rothman [1999], as described by Stohl *et al.* [2005]. Suspended dust mass can be modified by dry and wet deposition processes within FLEXPART. Dry deposition of particulate matter is calculated from a parameterization using dust particle size and density according to Slinn [1982]. Since different air parcels represent different dust particle sizes, dry settling moves air parcel trajectories toward the surface, which can be counteracted by upward directed winds. Moist deposition includes within-cloud and below-cloud scavenging and follows the scheme of Hertel *et al.* [1995]. More details on the dispersion and removal processes are available in the FLEXPART documentation for version 8.2 (www.flexpart.eu).

Calculated dust emission was determined using the same principles as used in common grid-scale models. The off-line preprocessor DustBowl extracted wind speeds from the ECMWF analysis data and converted the information into a dust flux to the atmosphere following Tegen and Fung [1994]. More specifically, the total mass flux F_D in units of $\mu\text{g s}^{-1} \text{m}^{-2}$ for a 3 h time interval was determined for the bare-soil fraction f of each $0.25^\circ \times 0.25^\circ$ grid box according to the equation

$$F_D = C \cdot f \cdot (u - u_t) u^2 \quad (1)$$

where u is the wind velocity at 10 m, u_t is the threshold velocity (typically $6\text{--}9 \text{ m s}^{-1}$) [e.g., Chomette *et al.*, 1999], and C is a dimensional factor that is often determined a posteriori [Tegen and Fung, 1994]. Here we use the values $u_t = 6.0$ and $C = 0.7 \mu\text{g s}^2 \text{m}^{-5}$. While the values of u_t and C are not rigidly defined, the Tegen and Fung [1994] scheme has the advantage of being widely used and straightforward to implement. In the future, additional mobilization schemes, such as the more advanced Kok [2011] scheme, can be included in the DustBowl preprocessor.

The total mass flux per time interval was then used to build a dust initialization file for the FLEXPART model. Almost any desired initial particle size distribution (PSD) can be specified in FLEXPART. The particle size distribution at emission was chosen similar to the ground-based PSD measurements from d'Almeida and Schütz [1983]. More specifically, the initial PSD was obtained from a Junge distribution with exponent $\alpha = 1.5$, fitted to their dust storm case. In total, 15 size bins were selected, following the recommendations by Foret *et al.* [2006], in a range from 0.1 to $63 \mu\text{m}$ (Table 1). For the transport simulation, the total dust mass was first distributed into the 15 size bins with different mass fractions as given by Table 1. Then, the dust mass in each size bin was distributed equally between 2000 particles per 3 h interval to allow for spreading of the dust plume. The particles were randomly distributed between the surface and 500 m above ground to provide initial dispersion. For the emission periods identified here, this totaled about 60,000 particles per simulation. In addition, sensitivity studies were performed with respect to the parameters u and u_t in equation (1), the emission height, and the duration of the dust emission (see section 4.3).

When interpolating the ECMWF data to a lower resolution, the mean wind speed has been reduced at some grid cells. Lowering the threshold velocity is one possibility to account for this effect when calculating dust emission with the Tegen and Fung [1994] scheme. Another possibility is to consider wind gustiness instead of wind speed. As discussed by Morcrette *et al.* [2008] and as apparent from equation (1), dust mobilization is strongly nonlinear, and thus, in reality, short-term wind gusts may have a disproportionately large impact on total dust emission. To investigate the potential influence of wind gustiness on dust mobilization, experiments are performed here using the parameterized gustiness from the ECMWF model. This variable represents the maximum wind in a 1 h period and is calculated as the

Table 1. Dust Size Categories Used in the FLEXPART Simulations^a

Species	Size Bin Lower Edge (μm)	Size Bin Upper Edge (μm)	Geometric Mean (μm)	Mass Fraction (%)
1	0.1	0.6	0.30	0.001
2	0.6	1.6	1.05	0.009
3	1.6	2.5	2.02	0.021
4	2.5	3.8	3.12	0.058
5	3.8	4.7	4.24	0.063
6	4.7	5.7	5.19	0.094
7	5.7	7.5	6.58	0.243
8	7.5	9.0	8.24	0.282
9	9.0	12.0	10.50	0.812
10	12.0	14.5	13.20	0.958
11	14.5	26.0	20.00	8.400
12	26.0	35.0	30.40	12.100
13	35.0	41.0	38.00	11.200
14	41.0	50.0	45.40	21.900
15	50.0	63.0	56.40	43.900

^aMass fractions for Junge distributions from 0.1 to 63 μm , exponent $\alpha = -1.5$, based on the sand storm data from d'Almeida and Schütz [1983].

sum of a stability-dependent turbulent gustiness, plus a parameterized convective gustiness [Bechtold and Bilot, 2009]. Convective gustiness is calculated from the low-level wind shear between 850 and 950 hPa in grid cells where convection is active. When calculating the total mass flux using gustiness instead of the mean wind, an empirical scaling factor is included in equation (1) to account for the nonstationarity of the mobilization from gusts. Morcrette *et al.* [2008] used a scaling factor of 0.5 in their mobilization calculations. Here we use a value of 0.1 to match the maxima of dust mobilization resulting from both sets of calculations.

3. Observed Dust Mobilization and Transport

3.1. Meteorological Conditions During Dust Mobilization

Climatologically, during June, the meteorological situation in central western Africa is characterized by the interplay between the Saharan Heat Low (SHL) and the West African monsoon. The intertropical discontinuity (ITD) is the surface air mass boundary separating the moist low-level monsoon southwesterlies from the dry and hot air masses of the Sahara desert transported with the Harmattan [Lafore *et al.*, 2011]. At this time of the year, the ITD is typically located at 20°N west of the Tibesti Mountains, with the SHL located just to north of it [Lavaysse *et al.*, 2009]. Large MCSs can form in association with monsoon surges south of the ITD [Couvreur *et al.*, 2010]. As has recently been suggested, the MCSs may thereby contribute to initiating African easterly waves (AEWs), which in turn may be associated with further moist convective activity during their baroclinic development phase [Berry and Thorncroft, 2005; Hall *et al.*, 2006]. Dust may be mobilized and transported with monsoon surges in complex ways, both within and at the leading edge of the monsoon flow [Bou Karam *et al.*, 2008]. In addition, MCSs can trigger the mobilization of dust within haboobs, that is, at the leading edge of cold pools emanating below the clouds due to evaporating rainfall, thereby often extending over hundreds of kilometers [e.g., Flamant *et al.*, 2009a, 2009b]. Knippertz and Todd [2010] confirmed from case studies and a satellite-based statistical analysis that AEWs are important for enhanced atmospheric dust load in the central western Sahara during summertime because of moist convection and the surface signature of AEW vortices. Mobilization due to haboobs was clearly evident several times during the Fennec period in June 2011 at BBM [Marshall *et al.*, 2013; Allen *et al.*, 2013]. The SHL during the study period was located close to 15°E before 12 June and then moved to 12°W thereafter, as during the case studied here [Todd *et al.*, 2013]. Lavaysse *et al.* [2009] identified the SHL position climatologically using the low-level atmospheric thickness between 925 and 700 hPa. We identify the SHL from sea level pressure (SLP) contours which for the purpose of this study provides a clear localization of the SHL center. In general, the view gained from considering SLP is consistent with the Lavaysse *et al.* [2009] method (not shown).

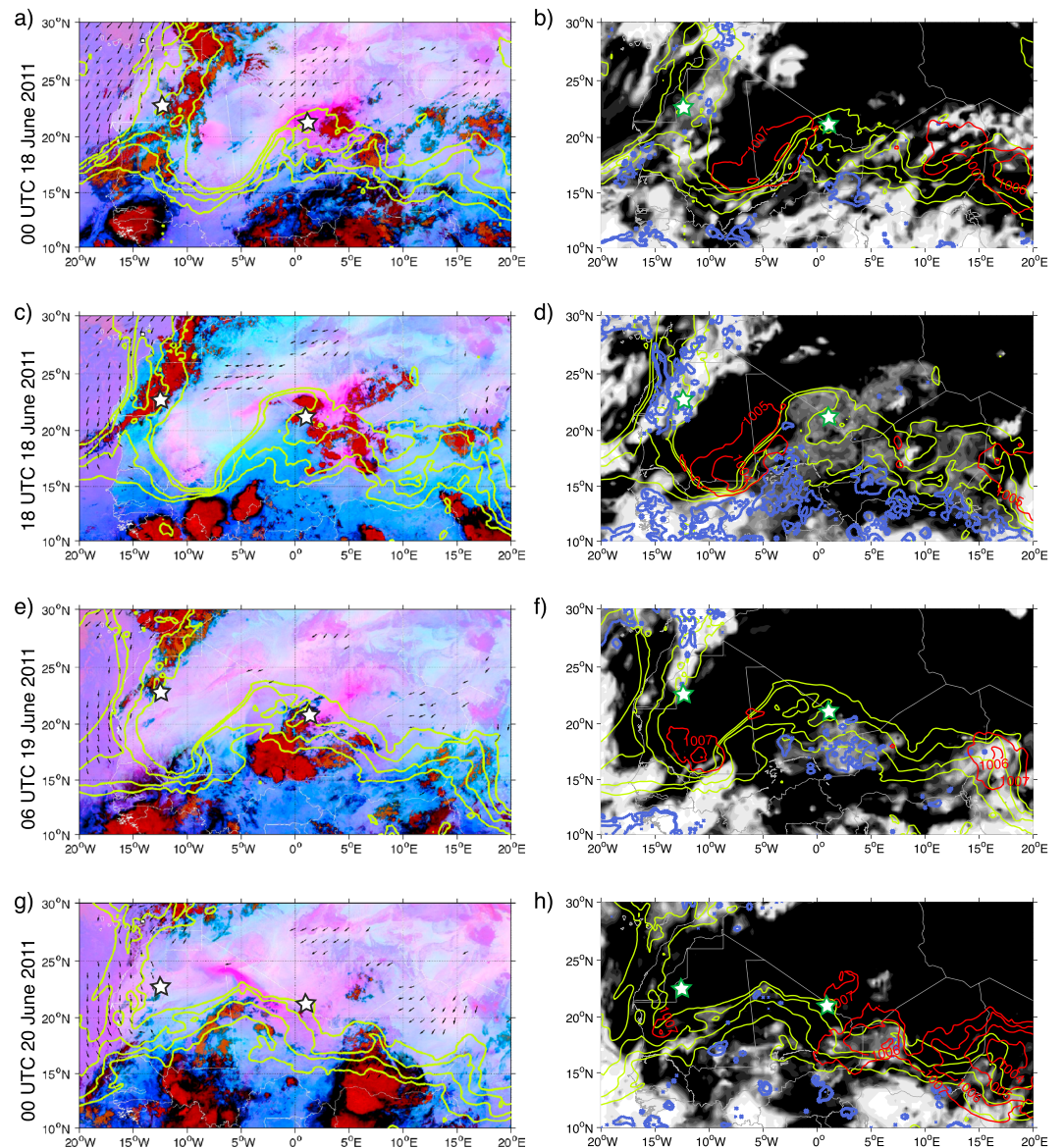


Figure 2. Meteorological conditions of dust emission at (a, b) 0000 UTC on 18 June 2011, (c, d) 1800 UTC on 18 June 2011, (e, f) 0600 UTC on 19 June 2011, and (g, h) 0000 UTC on 20 June 2011. Left column: MSG SEVIRI “dust RGB” images overlaid with IWV (light green; 25, 30, 35, 40 mm) and 10 m winds larger than 6 m s^{-1} (black arrows) from ECMWF analysis. Right column: ECMWF analyses of total cloud cover (shading, black is cloud free), sea level pressure (red contours, every 1 hPa), and total precipitation (blue contours; $0.1, 0.5, 1.0 \text{ mm } 3 \text{ h}^{-1}$). IWV contours are repeated in the right column for reference. White stars denote the Fennec supersites 1 and 2 (see Figure 1).

At 0000 UTC on 18 June 2011, the ITD showed a southward excursion over southern Mauritania and central Mali with a strong NS oriented gradient (green lines in Figures 2a and 2b). Toward eastern Mali and Niger, the ITD was more zonal and showed a weaker gradient, whereas east of 0°E the ITD gradient became meridional again. Morocco and the very northwest of Mauritania were under the influence of inflow from the North Atlantic [Todd *et al.*, 2013]. The SHL was split into a western center and eastern center of minimum SLP on that day (Figure 2b, red contours). The western center was located near the strongest humidity gradient of the ITD at $\sim 5^\circ\text{W}$. Low-level winds above 6 m s^{-1} were directed across central Algeria toward the region of the heat low (Figure 2a, black arrows at $\sim 0^\circ\text{W}$). In southern Algeria, intense pink colors indicate the presence of dust above $\sim 1.5 \text{ km msl}$ near the BBM site (star in Figure 2a). In this region, deep convection had developed and triggered large cold pool outflow during the previous day, which had moved into

southern Algeria and eastern Mali during the night. Note that the higher total column water masks the dust signal south of the ITD in the SEVIRI image by a dominant deeper bluish tint [Brindley *et al.*, 2012]. The deep red colored area just east of BBM (near 4°E) indicates remnants of convective clouds, which are not represented in the ECMWF analysis cloud field (Figure 2b). Otherwise, the cloud structures and the ITD signature agree fairly well between the SEVIRI imagery and the ECMWF analysis. An animation of the dust RGB imagery for the period 18–20 June 2011 is available as supporting information.

The western heat low intensified during the afternoon of 18 June, and its maximum shifted south to 15°N, 8°W (Figure 2d). Moist air advanced from southerly directions to the east of the SHL maximum, and clouds formed along the ITD between southern Algeria and northern Mali after 1400 UTC (Figure 2c). This cloud formation is apparent in both the ECMWF analysis and SEVIRI imagery, albeit with weaker intensity and further west in the analysis data (Figures 2c and 2d). Convection intensified in the late afternoon, and a cold pool became apparent below isolated convective cells at 2000 UTC (not shown). Further organization of the isolated convective cells into a squall line took place thereafter, triggering new cloud formation at its western edge.

At 0600 UTC on 19 June 2011, a coherent MCS is apparent over central Mali (Figure 2e). Several smaller cold pools merged and are visible as a distinct airmass boundary near 5°W, 20°N and extending northward from the western leading edge of the main cloud mass. The high total column humidity shifts the false-color image toward blue, possibly obscuring the presence of dust. In the ECMWF analysis, the MCS is not present, and only an area of weak cloudiness is evident between 0° and 5°E (Figure 2f). Interestingly, IWV in the ECMWF analysis data increased very markedly over central Mali between 1800 UTC on 19 June and 0000 UTC on 20 June, possibly indicating that humidity was underestimated in the analysis in this region at the earlier time, prohibiting a stronger convective development. No moist convective development was apparent after 0000 UTC on 20 June (not shown).

During 19 June, the MCS moves slowly in west-south-westward direction (Figure 2g). The SLP minimum of the SHL is being filled up and decays toward the evening (Figure 2h). The dusty cold pool front continues to move northwestward and then begins to come under the influence of low-level NE winds from central Algeria. At this time, the daytime deepening of the convective boundary layer (CBL) has mixed the dust into a deeper layer, leading to intense pink colors (Figure 2g). Advection into an overall drier region of the Sahara may have further increased the color intensity [Brindley *et al.*, 2012]. The dusty cold pool air has been distorted into a hook-like shape with its tip bending toward Mauritania. The “dust RGB” images show a strong intensification of the pink color as the dust front enters the Erg Chech near 24°N, 5°W, again possibly indicating intensified dry convective mixing of dust. In addition, some dust may be mobilized from small paleolakes located north and south of Erg Chech [Ashpole and Washington, 2013, Figure 5]. The tip of the dust plume starts fanning out thereafter and moves further west during 20 June into the range of operation of the two research aircraft while maintaining a more or less coherent shape (shown in detail in section 4.3).

Automatic weather station 134 shows the passage of the cold pool in several meteorological variables just after 0100 UTC on 19 June 2011 (Figure 3). A pressure jump of ~1 hPa marks the arrival of the density current (Figure 3c, solid line). Wind speed shows a simultaneous signal of the arrival of the dust front, as mostly calm conditions change to moderate winds from the southeast with gusts up to 6 m s^{-1} after 0100 UTC (Figures 3b and 3c). Temperature shows a delayed increase, reaching 3–4 K shortly after the surface pressure maximum (Figure 3a, solid line), indicating that the relatively warmer air of the density current is mixing down through the colder stable boundary layer to the surface [e.g., Hobby *et al.*, 2013; Heinold *et al.*, 2013]. The airmass at AWS134 continues to cool after 0200 UTC when winds have returned to calm conditions and northerly directions. The gradual increase in specific humidity from 2.5 to 5.0 g kg^{-1} indicates the arrival of a humid air mass between 0100 and 0200 UTC, again delayed with respect to the temperature signal. The humidity remains nearly constant at the station thereafter. These signatures are comparable to cold pool passages reported in earlier studies [e.g., Emmel *et al.*, 2010]. The temporal offset between specific humidity and pressure/temperature, respectively, noted here indicates that an undular bore may have preceded the arrival of the cold pool air (an undular bore is clearly visible in the supporting information). This is supported by the wind gusts decreasing jointly with temperature (Figure 3b, dashed line). It is not clear why wind gusts are already high before 0100 UTC.

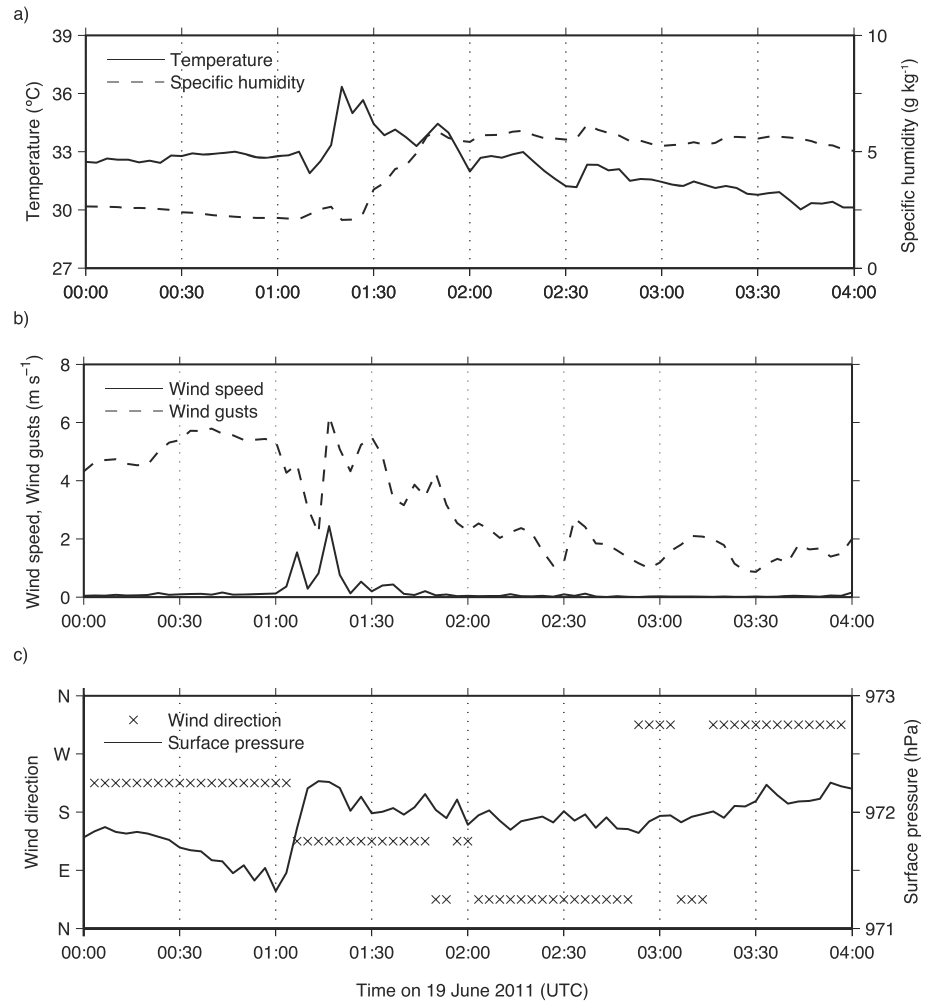


Figure 3. Time series of (a) temperature (°C, solid line), specific humidity (g kg⁻¹, dashed line), (b) wind speed (m s⁻¹, solid line), wind gusts (m s⁻¹, dashed line), (c) wind direction rounded to the nearest 90° sector (crosses), surface pressure (hPa, solid line) at AWS134 (see Figure 1 for location) for a nighttime cold pool passage at 0130 UTC on 19 June 2011.

3.2. Thermodynamic Properties of the Dust Plume

The vicinity of the targeted dust plume was characterized by a complex configuration of different air masses. IWV from ECMWF analyses (shading and contours in Figure 4) reveals a north-south oriented humidity gradient, which reflects the marked transition between the Saharan and monsoonal air across the ITD. Low-level inflow of cool and moist air extends as a tongue with an IWV of 18–22 mm in a northwestward direction near 9°W, 23°N. Surface winds at 10 m from the ECMWF analysis show that this moderately moist airmass was sheared cyclonically between the southwesterly monsoon flow and a fairly strong, dry (<14 mm IWV) easterly flow north of 23°N. The IWV minimum of <14 mm near 12°W, 24°N is the remainder of a very dry airmass that previously formed the center of the Saharan Heat Low (Figures 2f and 2h), and that has now been displaced to the west. While the Falcon 20 surveyed the synoptic to mesoscale environment in a triangular flight pattern (green track), the BAe-146 probed the vertical structure of the dust plume in detail along its southern boundary between points A and B (red track). Both aircraft together deployed 19 dropsondes along their flight tracks (black circled crosses and stars). The SEVIRI “dust RGB” product at the time of flight operations (Figure 4b) shows moist air in blue at the southern edge of the domain shown in Figure 4a (black dashed line) and a band of clouds coinciding with a region of lower surface albedo (Figure 4b, orange marker). The dust plume is evident as a broad pinkish area in the northwestern part of the domain, connected to a partly cloudy region in the east by a narrow dust

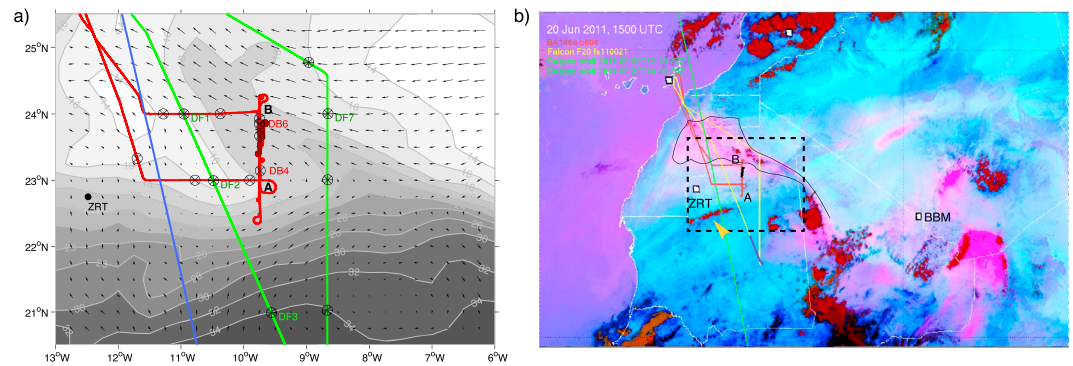


Figure 4. (a) Dropsonde locations and joint flight patterns of the BAe-146 (red) and Falcon 20 aircraft (green). Aircraft locations at 1500 UTC on 20 June 2011 ± 7.5 min are shown in darker color for the BAe-146. A CALIOP satellite overpass at 1415 UTC is denoted by the blue line. The ITD separating Saharan and monsoonal air is apparent from the IWV (shading, mm) and 10 m winds, both from ECMWF +3 h forecast data valid at 1500 UTC. A-B is the lidar transect analyzed for the BAe-146. Crossed circles denote dropsonde locations (only the ones discussed here are labeled). (b) Dust plume location from the SEVIRI “dust RGB” satellite product (colors) with a manually drawn outline (black) and overlaid flight tracks of the BAe-146 (red) and Falcon 20 (yellow) at 1500 UTC on 20 June 2011. Marker indicates moist air and clouds south of supersite 2 at Zouerate (ZRT). Thick segments show location of the aircraft ± 7.5 min at the time of the SEVIRI image. The dashed black box denotes the region covered by Figure 4a. Label BBM indicates location of supersite 1 at Bordj Badji Mokhtar.

zone along a convergence line. Isolated cumulus clouds are also apparent just northeast of point B (Figure 4b), in disagreement with the ECMWF analysis.

3.2.1. Mesoscale Thermodynamic Environment and Dust Structures

The eastern and western aerosol lidar curtains obtained along the flight legs of the Falcon 20 together with dropsondes complement the thermodynamic perspective gained from analysis and satellite data (Figure 5). The western transect, which was taken from north to south during 1405 to 1446 UTC, shows high concentrations of dust north of 24°N and intense extinction at up to 4 km msl (Figure 5a). The top of the CBL is fairly inhomogeneous and shows variability due to small-scale turbulence [Ryder *et al.*, 2015]. South of 23.7°N, this dusty airmass can be less clearly identified. Dropsonde #1 of the Falcon 20 aircraft (DF1) shows that the change in extinction at ~ 4 km msl is reflected in the humidity profile, identifying the layer above the CBL as a Saharan Residual Layer (SRL) [Cuesta *et al.*, 2009] from the previous day (see also Figure 6a). Surface temperatures are very high, reaching more than 44°C. The aerosol structure changes notably toward the location of DF2 ($\sim 23^\circ\text{N}$, Figure 5a). Extinction is lower, the CBL top is more uniform, and an additional aerosol layer appears near ~ 6 km msl. Even though DF2 indicates almost saturated conditions with respect to water at this altitude (Figure 6b), no clouds were apparent from an additional high-quality cloud product (not shown). Possibly, the strong extinction could have been caused by activated dust. South of 22.8°N, the CBL reaches higher altitudes and has grown into the residual layers. Cumulus clouds are evident farther south (see also Figure 4b, orange marker), probably favored by the moist monsoon inflow from further south as seen in Figure 4a, possibly also supported by the low-albedo region El Hank, favoring low-level convergence and stronger updrafts (Figure 4b) [Ryder *et al.*, 2015]. Well south of the ITD, where IWV exceeds 32 mm, dropsonde DF3 (Figure 5b) shows surface temperatures around 40°C, and clearly more humid conditions in the CBL persist with southerly inflow ($8\text{--}9\text{ g kg}^{-1}$, Figure 6c). Near-saturated conditions exist in layers with easterly flow between 4 and 6.5 km above sea level (asl).

Figure 5b shows the northbound lidar transect of the Falcon 20 further east. Again, cumulus clouds are apparent in a region between 21.7 and 22.8°N. South of 23.8°N, the atmosphere is nearly aerosol free above 6–7 km msl. Below, a residual layer is clearly visible, and a more aerosol-rich CBL with altitudes varying around 5 km msl. To the north of 23.4°N, a distinct change in the vertical structure is apparent, with stronger extinction showing a highly variable CBL top between 3 and 5 km msl and higher cumulus clouds north of 24°N. Dropsonde DF7, which directly sampled this cloudy airmass, clearly indicates more humid conditions than further west at the same latitude ($5\text{--}6\text{ g kg}^{-1}$ compared to 3 g kg^{-1} at DF1, see Figure 6d). Well-mixed conditions prevail up to 5.5 km msl, and some dust appears to have penetrated to

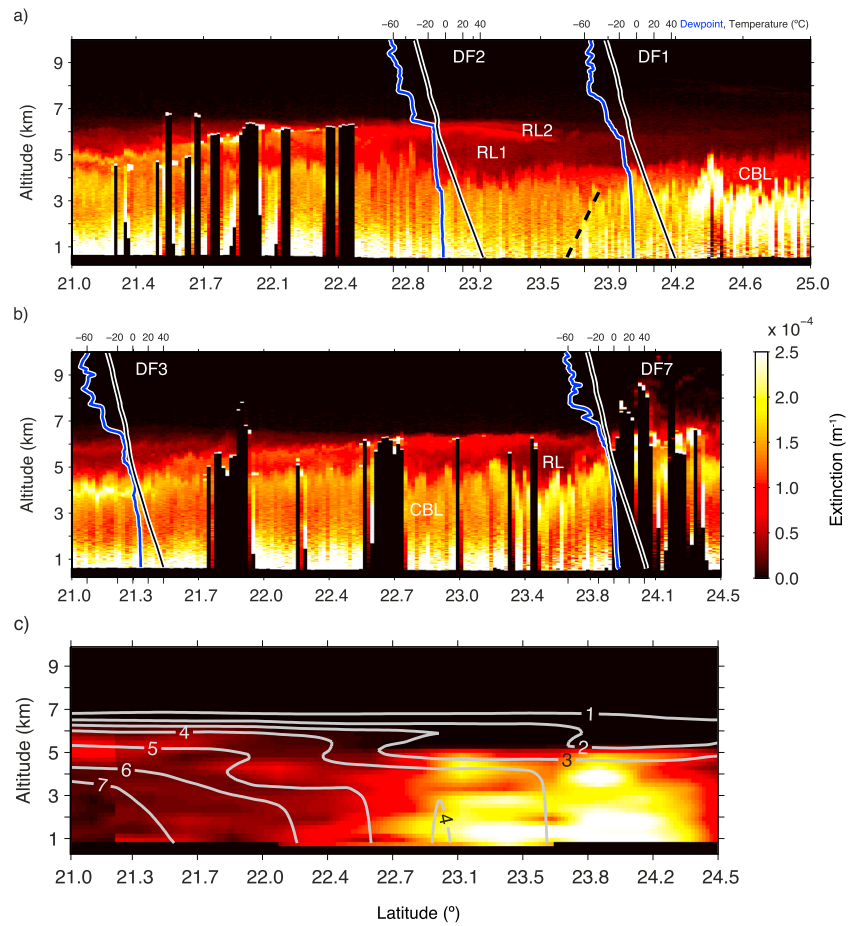


Figure 5. Falcon 20 lidar extinction curtain (m^{-1}) versus latitude (a) along the southbound transect west of the BAe-146 flight track and (b) along the northbound transect east of the BAe-146 flight track (see Figure 1 for orientation). Profiles of temperature (black, $^{\circ}\text{C}$) and dew point temperature (blue, $^{\circ}\text{C}$) from dropsondes DF1 to DF7 overlaid at approximate dropping locations. RL1, RL2 = residual layers, CBL = convective boundary layer. (c) Simulated aerosol extinction (shading, m^{-1}) for the northbound transect from FLEXPART Experiment 1, overlaid by specific humidity from ECMWF analysis data (white contours, g kg^{-1}). Figure 5c is discussed in section 5.3.

altitudes between 8 and 9 km msl in the vicinity of the cloud. Cumulus clouds are also apparent in the satellite imagery (Figure 4b, black marker). Specific humidity along the same transect in the ECMWF model (Figure 5c, white contours) shows enhanced moisture content to the south of 22.7°N , but not for the region north of 24°N , indicating that the ECMWF model does not contain enough moisture to form clouds near DF7. It seems that this moisture added to the desert boundary layer is important for deep mixing of the CBL, as suggested by earlier studies [Flamant et al., 2007; Marsham et al., 2013; Garcia-Carreras et al., 2013]. Here the humidity injected by moist downdrafts associated with the MCS or advected from the monsoon front may have played an important role in breaking up inversions at the boundary-layer top by enabling moist convection. Note that the shading in Figure 5c will be discussed in section 5.3.

3.2.2. Transect Across the Southern Boundary of the Dust Plume

The BAe-146 probed the vertical structure of the dust plume at its southern edge along transect AB (Figures 4a and 4b). Albeit at much lower resolution, the lidar retrieval along AB shows very similar structures as in the surrounding transects of the Falcon 20 (Figure 7a, compare Figure 5). A pronounced north-south gradient of extinction in the CBL is evident, with stronger dust concentrations to the north of $\sim 23.7^{\circ}\text{N}$. Further south, there is again a vertical separation into the CBL below and two residual layers RL1 and RL2 above (Figures 7a and 7b), which is apparent in comparison to Figure 5a. In the CBL, the depolarization plot at the northern end of the transect suggests the presence of less spherical and thus

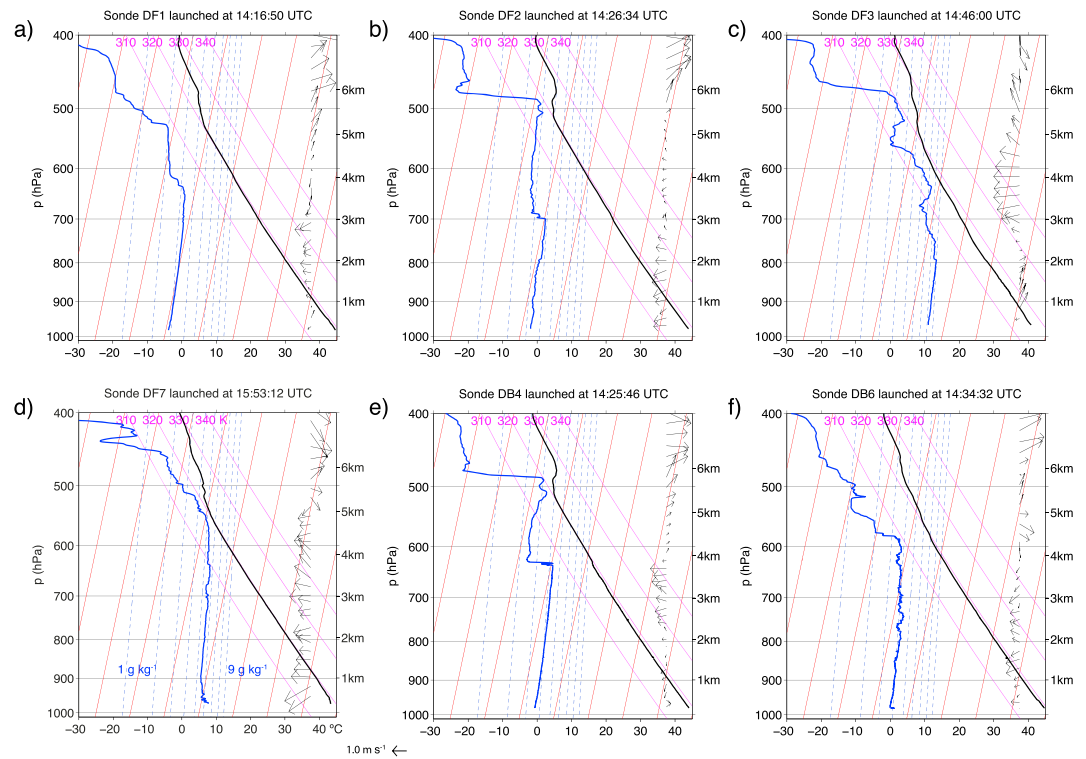


Figure 6. Vertical soundings from dropsondes launched during the flights on 20 June 2011 in skew-T-log-p diagrams at the locations indicated in Figure 4. Dropsondes launched (a–d) from the Falcon 20 and (e, f) from the BAe-146. Shown are air temperature (solid black line), dew point temperature (solid blue), and wind speed and direction (arrows) from the dropsonde measurements. Specific humidity can be inferred from the dashed blue coordinates. Reference arrow indicates 1.0 m s^{-1} .

coarser, recently uplifted dust. This agrees well with the interpretation of the satellite imagery indicating the southern edge of the dust plume about halfway along transect AB (Figure 4b).

Dropsonde #4 of the BAe146 aircraft (DB4), which is located at the southern end of the transect near A, shows the separation between a fairly dry CBL ($\sim 4 \text{ g kg}^{-1}$) topped by an even drier SRL ($2\text{--}3 \text{ g kg}^{-1}$, Figures 7a and 6e). At the top of the residual layer, the airmass is more humid and close to saturation, and clouds were observed at that location (Figures 7a and 7b, area marked with CL). Dropsonde DB6 at the northern end of the transect shows a CBL top near 4.5 km msl, which does not appear to be topped by a residual layer, but by the free troposphere above (see also Figure 6f). The humidity structure in the CBL is much less homogeneous than for dropsonde DB4, indicating less complete mixing, while the humidity is similar with a mixing ratio of $\sim 4 \text{ g kg}^{-1}$. Along this transect, the humidity in the CBL may not suffice to overcome the inversion at the CBL top as seen at dropsonde DF7 (Figure 6d). Note that Figure 7c will be discussed in section 5.3 together with Figure 5c.

Along transect AB, a complex flight pattern was performed with the BAe-146 to obtain in situ measurements of aerosol properties within the lidar curtain (Figure 8c). The center panel of Figure 8 shows the slantwise descent of the aircraft at point B in black, a low-level run at minimum safe altitude ($\sim 350 \text{ m}$ above ground level (agl)), and a slantwise ascent at point A, before obtaining a second lidar curtain along the transect AB. All lidar data were obtained at 8 km asl. An averaged lidar profile along the flight segment at point A is shown by the thick line in Figure 8a. There is good correspondence with the extinction profile from the onboard nephelometer down to 2 km asl (Figure 8a, thin solid line), whereas further below the lidar data have a poor signal-to-noise ratio. At point B, there is good agreement between the two extinction measurements down to about 3 km asl (Figure 8b). Figure 7a suggests that the lidar is attenuated by the large dust concentrations in the atmosphere below 2–3 km asl at 23.9°N. Below 1 km asl, the nephelometer indicates very strong extinction, exceeding $17.1 \times 10^{-4} \text{ m}^{-1}$ (Figure 8b). The low-level transect (Figure 8d) shows a pronounced

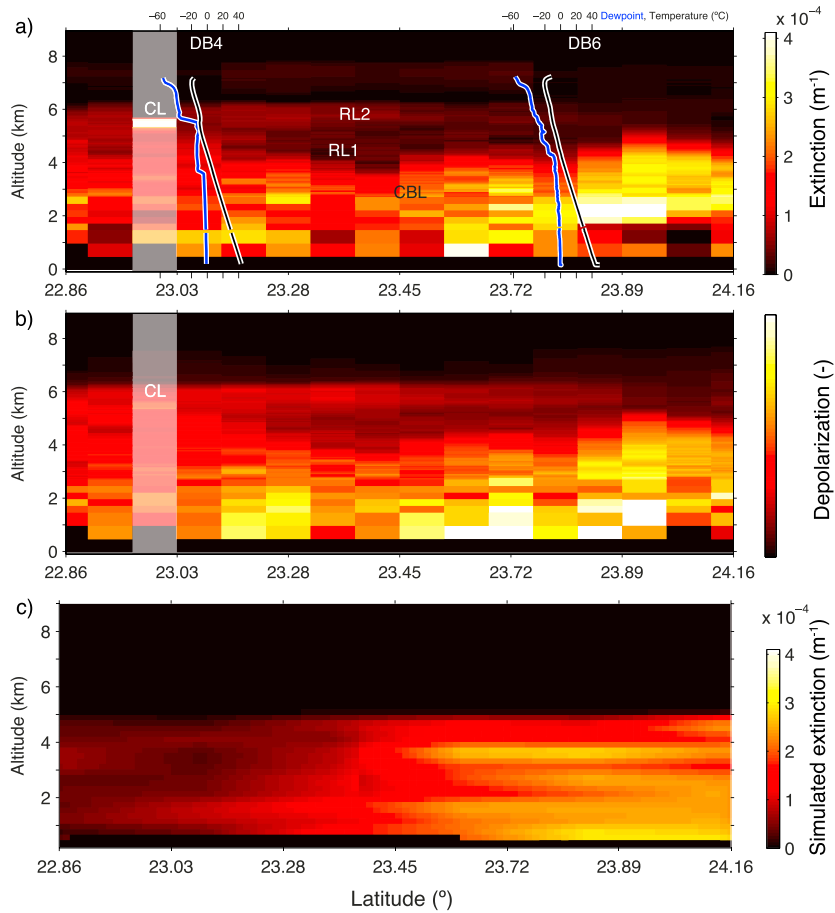


Figure 7. BAE-146 lidar curtain along transect AB for the time period 1423 to 1438 UTC on 20 June 2011. (a) Aerosol extinction (m^{-1}) with profiles of temperature (black, $^{\circ}\text{C}$) and dew point temperature (blue, $^{\circ}\text{C}$) from dropsondes DB4 and DB6 overlaid at approximate dropping locations. RL1, RL2 = residual layers, CBL = convective boundary layer, CL = cloud. (b) Depolarization in arbitrary units (for qualitative purposes only—no quantitative scale is provided). (c) Simulated aerosol extinction (m^{-1}) along the same transect from FLEXPART Experiment 1. Figure 7c is discussed in section 5.3.

gradient from high extinction at the northern end of the transect at point B with values of $6\text{--}8 \times 10^{-4} \text{ m}^{-1}$ changing toward values of $3 \times 10^{-4} \text{ m}^{-1}$ below point A.

A value for extinction was also obtained from the size-resolved aerosol mass profiles. Total aerosol concentration c , given by the sum of the accumulation, coarse, and giant mode mass loading, was scaled to extinction α based on a relation given by *Marenco et al.* [2011]:

$$\alpha = c \times k_{\text{ext}} / f \tag{2}$$

We assumed a dust fraction of $f_c = 1.0$ and used the mass-specific extinction coefficient $k_{\text{ext}} = 0.48 \text{ m}^2 \text{ g}^{-1}$ as determined by *Johnson and Osborne* [2011] during the GERBILS campaign (including coarse mode particles). The dashed lines in Figures 8a and 8b show the extinction values derived from this procedure (denoted as PSD). There is reasonable agreement with the nephelometer and lidar extinction estimates, yet substantial underestimation is apparent at point A and partial overestimation and underestimation at point B. It is possible that differing relative contributions from the three size fractions prevent this simple scaling or that the nephelometer is biased to a size fraction below $2.5 \mu\text{m}$ [*Ryder et al.*, 2013a]. Note that k_{ext} ranges between 0.13 and 1.22 for different measurement campaigns [*Johnson and Osborne*, 2011; *McConnell et al.*, 2008], but the best agreement was found for the value of k_{ext} used here. Larger particles will act to reduce k_{ext} , as they are less efficient at extinguishing light per unit mass compared to small ones, which would negatively affect the comparison made here when included. Deviations from this linear relationship

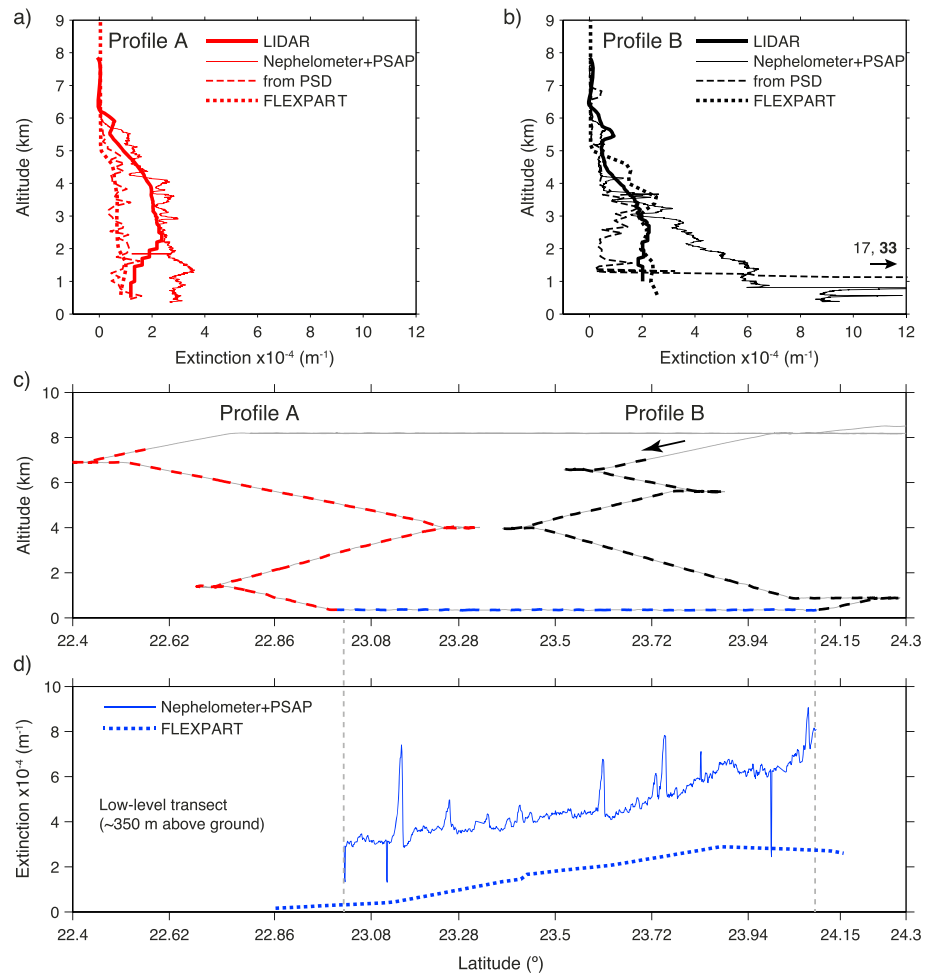


Figure 8. Extinction measured by lidar and nephelometer + PSAP at 550 nm during flight b604 along transect AB. (a) Extinction from lidar (thick solid line), nephelometer + PSAP (thin solid line), and calculated from measured PSD (dashed line) during ascent at point A. (b) As before, but during descent at point B. (c) Flight profile along transect AB. Colors denote flight segments in matching colors (red for profile at A, black for profile at B, blue for low-level transect AB). (d) Extinction derived from nephelometer + PSAP during a low-level run at approximately 350 m above ground.

according to equation (2) are also to be expected in the presence of clouds, that is, near the Saharan planetary boundary-layer (PBL) top where relative humidity is likely to modify the dust optical properties through absorption of water [Hänel, 1976].

4. Dust Mobilization and Transport Simulations

As presented in the previous section, a wide range of very detailed aircraft measurements have been obtained along the dust gradient in the area of operations. This provides excellent conditions for determining anticipated dust sources and transport patterns using the Lagrangian particle dispersion model FLEXPART. While dust in residual layers had a more aged appearance, dust within the CBL was—according to satellite imagery—advected into the region of aircraft operations up to ~40 h after having been mobilized. A successful numerical simulation of the dust feature sampled by the two research aircraft thus requires two components: (i) a realistic representation of the dust mobilization, initiating atmospheric dust concentrations, and (ii) a realistic representation of the mesoscale wind fields and dry convection which determine the dust transport. First, it is shown that a direct forward calculation of dust emission will not be successful for the case studied here because of deficiencies in the meteorological analyses. However, the satellite observations sufficiently constrain the dust transport aspect of the simulations. This

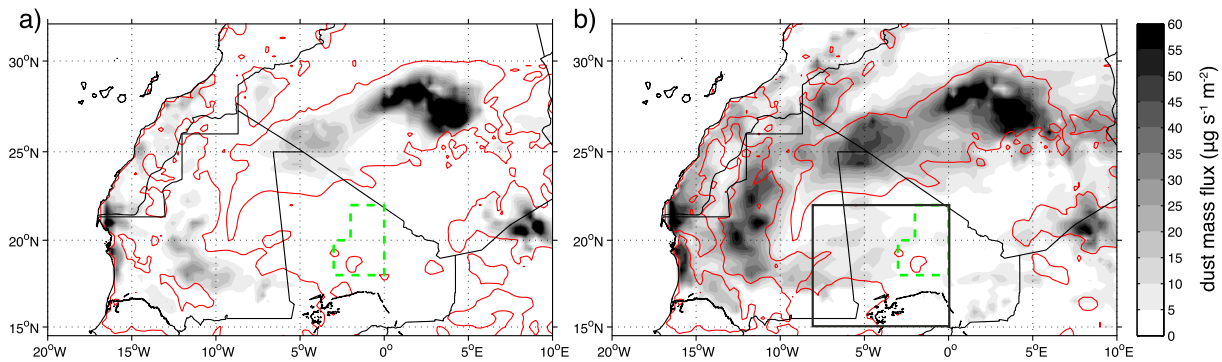


Figure 9. Average surface dust mass flux calculated from ECMWF analysis data between 1800 UTC on 18 June 2011 and 1500 UTC on 19 June 2011 (a) using 3-hourly 10 m mean winds, (b) using the 3-hourly parameterized 10 m wind gusts (shading, $\mu\text{g s}^{-1} \text{m}^{-2}$). Thin red contour denotes the area where the 10 m wind speed exceeds 6 m s^{-1} at least once during the mobilization period. Green dashed contour outlines region where mobilization due to MCS cold pools occurred according to satellite imagery (see Figure 2e). Black box denotes region from where dust mobilized by gustiness was initialized.

allows us to obtain an effective dust source, which then allows us to study the sensitivity of the dust model to source parameters.

4.1. Dust Mobilization Calculated From ECMWF Analyses

Dust mobilization for initializing the FLEXPART dust transport model is first calculated using equation (1) with 10 m mean winds from ECMWF analysis data for the period during which dust appeared to emanate below the MCS in dust RGB satellite imagery (see Figures 2c and 2e). The total accumulated dust mobilization from 1800 UTC on 18 June to 1500 UTC 19 on June 2011 is concentrated in areas below the northeasterly low-level jet across central Algeria and in southern Mauritania (Figure 9a, gray shading). The fact that it appears directed toward the SHL in southern Mauritania suggests that this mobilization is mainly caused by persistent mesoscale winds (see also wind arrows in Figures 2a and 2c). This is further supported by the areas where the 10 m wind speed exceeds the threshold velocity of 6 m s^{-1} at least once during the mobilization period (red contour). Notably, no dust mobilization is apparent in most of northern Mali, in particular in the regions where the MCS appears in the satellite imagery (Figure 9a, green dashed area, see also Figures 2c and 2e). A FLEXPART simulation initialized with the dust mobilization depicted by the gray shading in Figure 9a does not provide a useful reproduction of the observed dust plume (not shown).

To test whether the mobilization was affected by low grid resolution and thus low 10 m mean winds in relation to the threshold velocity u_t or by too weak convection in the analysis data compared to observations, dust mobilization using equation (1) was also calculated using the 10 m wind gustiness from the ECMWF analysis data as described in section 2.3 (Figure 9b). Dust mobilization for this parameter is generally consistent with the result obtained from the 10 m mean winds, but of markedly larger magnitude. Dust mobilization now also extends into regions not bound by the red contour (regions where 10 m winds exceed the threshold velocity at least once during the mobilization period). There is still no substantial dust mobilization in the MCS region (Figure 9b, green dashed contour), apart from a region west of the MCS domain with a mass flux of $5\text{--}10 \mu\text{g s}^{-1} \text{m}^{-2}$. This indicates that the gustiness was not related to moist convection in the MCS region, underlining the fact that the analysis did not contain sufficient rainfall to mobilize dust. A substantial part of the gusts in Figure 9b is probably related to the 0900 UTC low-level jet breakdown that is not captured by 6-hourly analyses [Knippertz, 2008]. Consequently, a simulation initialized only with the dust mobilization inside the region west of the MCS area (black box in Figure 9b, $15\text{--}22^\circ\text{N}$, $8\text{--}0^\circ\text{E}$) does contain a dust plume (not shown).

Clearly, the simulated dust mobilization does not match with the large dust plume apparent in this region in the satellite imagery, because the deep moist convection is not well represented in the analysis data (Figure 2). In particular, in Figures 2e and 2f, it can be seen that the MCS moving gradually to the southwest near 0°E is almost absent from the ECMWF data. Instead, precipitation from midlevel unorganized clouds near 4°E appears in the analysis (Figure 2f). Consequently, the cold pool from the observed MCS is also missing, as well as the associated pressure gradient driving the mobilization of dust

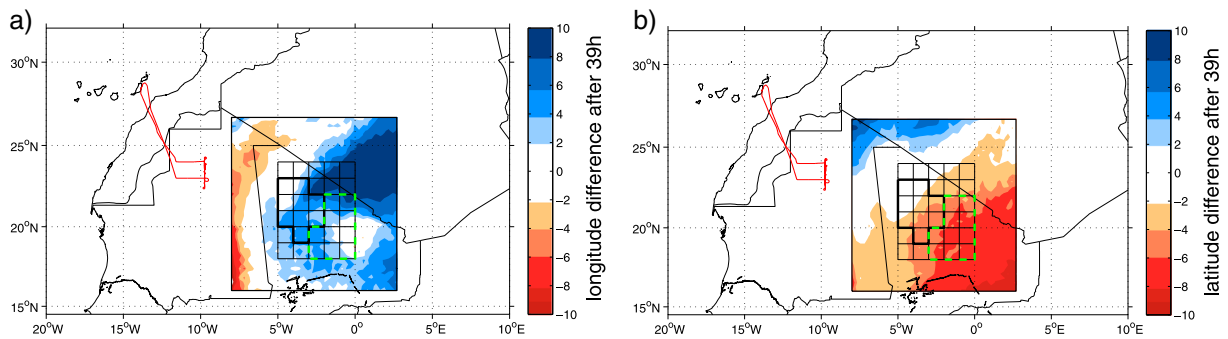


Figure 10. (a) Simulated dust longitude difference to the target region after 39 h forward calculation averaged over 3 h (at 1500 UTC on 20 June 2011). (b) Simulated mean dust latitude difference to the target region after 39 h forward calculation. Green dashed line indicates the region where dust mobilization below the MCS is apparent in the satellite imagery. Thick black contour indicates the dust mobilization region used for the manual sensitivity experiments. Only dust mobilized in the dust mobilization region from white shaded areas for both quantities arrives within the area of aircraft operations at the end of the simulation period.

and advection over hundreds of kilometers. Being run at a spectral resolution of T1279 (corresponding to an interpolated grid spacing of ~ 16 km), the current ECMWF model should be able to produce cold pools [Weisman *et al.*, 1997; Marsham *et al.*, 2011]. Note, however that Solomos *et al.* [2012] even used horizontal grid spacings down to 800 m for a detailed cold pool simulation in a regional model. More importantly, the representation of moist convection in the model and/or the sparsity of observational data in the region are likely responsible for the absence of the cold pool in the analysis data. Current parameterization schemes do not resolve updrafts/downdrafts and fail to reproduce the organization of moist convection into larger complexes. Interestingly, in addition, an AEW was forming near 3°E at that time [Todd *et al.*, 2013, Figure 3b]. AEWs are still notoriously difficult to predict due to their interaction of barotropic and baroclinic development [Bery and Thorncroft, 2005] and may thus also have contributed to the deficiencies in the ECMWF analyses in the present case.

4.2. Regional Dust Transport Properties

While the dust mobilization itself is not represented well, the mesoscale winds leading to the regional transport of the emitted dust toward the area of aircraft observations during the following 1–2 days are contained in the analysis. While a direct forward simulation of dust emission from the observed dust source will fail in this case, a simulation which inverts the observed dust patterns into an effective emission region providing the best possible match will provide insight into what aspects of the case were well represented, how large the dust emission should have been, and how sensitive the dust simulation is to changes in these parameters. We thus use the FLEXPART model to obtain dust transport properties first, which constrain the effective source region, and then prescribe dust emission over central Mali at locations from which we know that the dust will be transported to the target region. The sensitivity of the atmospheric dust load simulated by FLEXPART can then be evaluated in terms of the sensitivity to emission parameters at the source.

To identify the locations at which dust needs to originate, we extract transport properties from a dedicated Lagrangian forward simulation. We calculate the advection of 50,000 air parcels from the layer between 0 and 4 km agl in the domain 8°W – 3°E , 16°N – 27°N at 0000 UTC on 19 June 2011 for 39 h forward in time. The latitude and longitude at the corresponding arrival points are recorded and displayed as the difference between the air parcels' longitude at the end of the simulation and the aircraft transect AB longitude of 9°W (Figure 10a, shading). Dust mobilized in the white area within the boxed region in Figure 10a (small difference values) will reach the target longitude after 39 h. Dust originating in the red shaded regions will be transported too far toward the west, whereas dust mobilized in the blue shaded regions will remain too far east. The same interpretation applies for the difference from the target latitude of the transect at 23.5°N , which is shown in Figure 10b. Here dust originating in the blue regions is transported too far to the north, and dust from the red regions ends up too far south. Thus, the area where both quantities in Figure 10 are shaded white (~ 4 – 5°W , 22 – 23°N) is the mobilization area for the head of the dust plume reaching transect AB, whereas the regions further to the southeast are suitable mobilization regions for the trailing body of the dust plume, as apparent from Figure 4b.

A further step is required to identify the exact region where dust should be mobilized in terms of an effective dust source such that the visually best matching dust plume can be obtained. This approach bears similarity to inverse methods. In total, 20 individual FLEXPART simulations with dust released at neighboring $1^\circ \times 1^\circ$ grid cells in the lowermost 4 km msl during 0000 to 1200 UTC on 19 June 2011 were carried out within the region 6°W to 2°W and 19°N to 23°N (black grid shown in Figure 10). The wind speed is assumed to be homogeneous at 20 m s^{-1} , resulting in a dust mobilization of 169.3 g m^{-2} for a threshold velocity of 6.0 m s^{-1} according to equation (1). Sensitivity experiments modifying this value are described in section 5. The dust from each grid cell is then advected for 40 h forward in time using the FLEXPART model as described in section 2.3. Dust plumes from the individual simulations are combined by adding and removing initialization grid cells until the best visual agreement with the shape of the plume in the dust RGB satellite imagery is obtained. The resulting dust source region estimate is denoted by nine grid cells, bounded by the thick black contour in Figure 10. Interestingly, the region identified for manual initialization this way is located $\sim 200 \text{ km}$ northwest of the region where the large aging cold pool was seen to first emanate in the dust RGB imagery.

4.3. The “Best Match” Simulation

The dust plume resulting from this combination of single-cell dust simulations (henceforth referred to as “best match” simulation) is shown in Figure 11. At 1200 UTC on 19 June 2011, the dust plume covers most of northern Mali and is bound by sharp fronts toward north Mauritania in the west (Figure 11a, marker). At the corresponding simulation time $T+12$, the simulated dust plume has progressed northward from the initialization area (Figure 11b), covering approximately the same region as in the satellite imagery. Due to the southern limit of the dust initialization region, the western front of the simulated dust plume extends less far south than observed. The north-south dust concentration gradient apparent in the satellite imagery is not reproduced by the simulation due to the homogeneous initialization. To some extent, the observed gradient could be an artifact of the increasing moisture content in the atmosphere.

Six hours later, at 1800 UTC on 19 June 2011, the observed dust plume starts to form a westward pointing head, separated by a narrower neck from the body of the dust plume (Figure 11c, marker). The motion of the plume as a whole has slowed down except for the very southwestern end of the dust front, which continues moving westward. The formation of a head-and-neck structure is well reproduced by the FLEXPART simulation at $T+18$ (Figure 11d). The 700 hPa wind vectors in Figure 11d underline that the Harmattan flow from western Algeria is causing this deformation of the dust plume.

The deformation of the dust plume continues during the following 6 h. At 0000 UTC on 20 June 2011, the head has progressed slowly further west, and the neck has become even narrower (Figure 11e, marker). The dust front in the southwest coincides with high-altitude clouds, indicating that wet deposition may occur over southern Mauritania. The simulation at $T+24$ again matches the observed pattern of the dust plume (Figure 11f). The head starts to fan out over northeastern Mauritania. The narrowing neck appears to be due to a calm region just east of the initialization region (6°E , 22°N). It can clearly be seen that the simulated dust concentration is too large over the initialization region; hence, a considerable share of the mobilized dust has not been transported away from the emission region due to absence of the density current from the wind field.

Five hours before the flight operations, at 0900 UTC on 20 June 2011, the head of the dust plume has spread out over a large region in northern Mauritania (Figure 11g, marker). The body of the dust plume has collapsed into a narrow tail. In the corresponding simulation at $T+33$, the head of the dust plume is too far east, and too small (Figure 11h). Nevertheless, the location of the northern and southern boundaries at transect AB agrees well with observations. The good representation of the dust plume shape throughout the simulation underlines both the quality of the winds in the ECMWF analysis at the mesoscale and the ability of the FLEXPART model to simulate dust transport based on the model winds. The quantitative information on dust amount inside the plume from the in situ aircraft measurements is used in the following section to further constrain emissions at the dust source.

5. Comparison of the Simulation Result With Observations

Given that the transport after emission from the source has been simulated realistically, which has been supported by the findings in the preceding section, the dust concentration from the “best match”

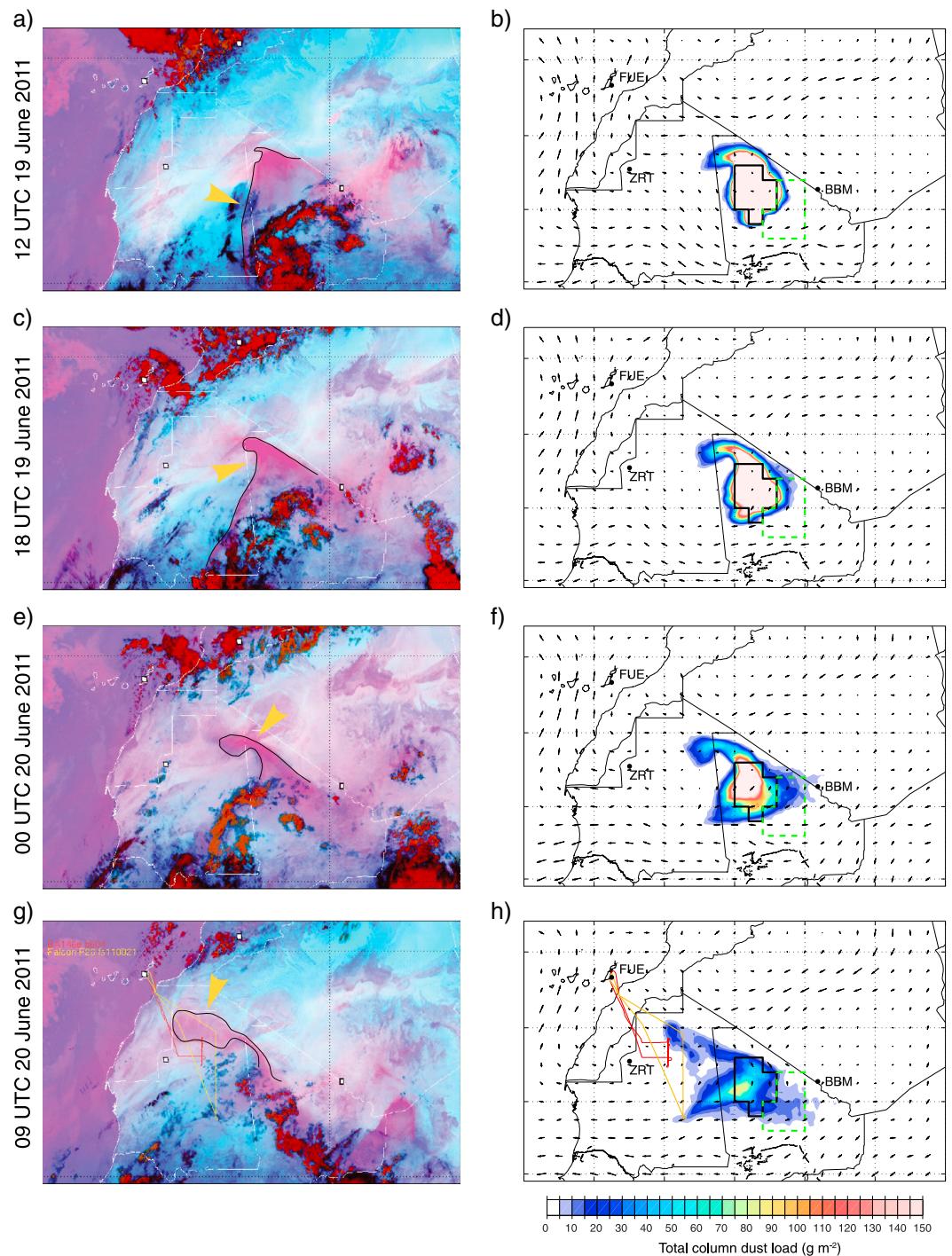


Figure 11. Time evolution of the observed plume in the SEVIRI “dust RGB” product (left column) and the total column dust load of the best matching manually initialized FLEXPART simulation Experiment 1 (right column). Dates are (a, b) 1200 UTC on 19 June 2011, (c, d) 1800 UTC on 19 June 2011, (e, f) 0000 UTC on 20 June 2011, and (g, h) 0900 UTC on 20 June 2011. In the right column, wind vectors at 700 hPa at a $1^\circ \times 1^\circ$ resolution indicate the main transport direction. In the right column, the thick black contour indicates the manual dust mobilization area, green dashed contour the MCS region. Flight tracks and supersite locations are given for reference in Figures 11g and 11h.

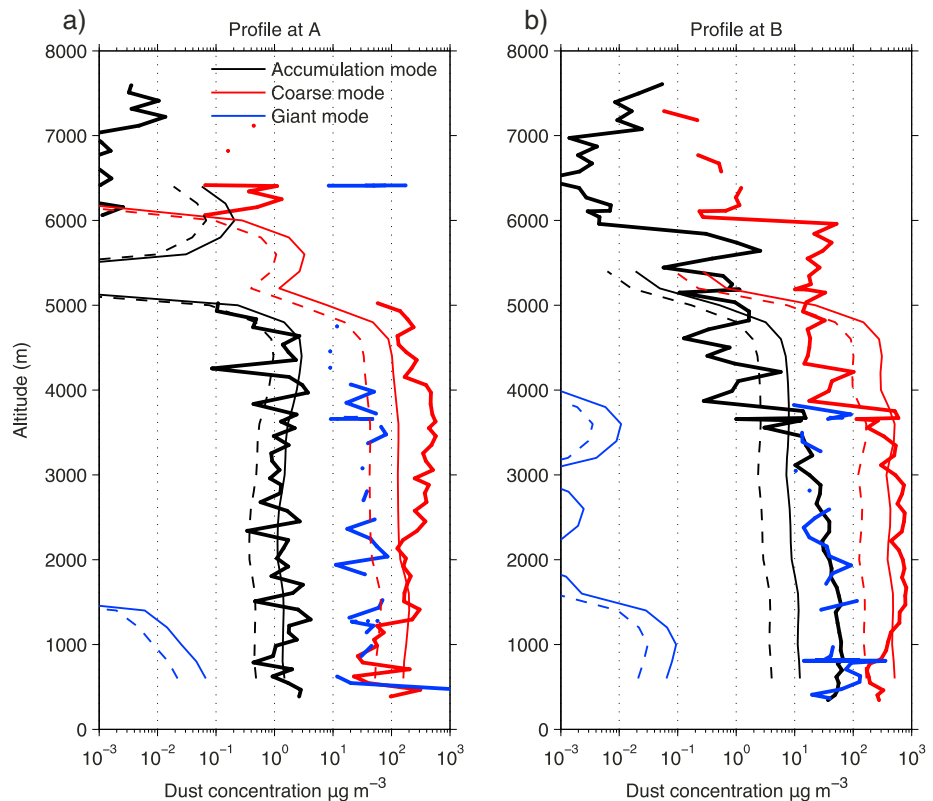


Figure 12. Vertical profiles of dust mass concentration from in situ aircraft measurements and FLEXPART simulations (a) at point A and (b) at point B along the BAe-146 transect AB (see Figure 4 for location). Black: accumulation mode, $d < 3 \mu\text{m}$, red: coarse mode, $d = 3\text{--}30 \mu\text{m}$, blue: giant mode, $d > 30 \mu\text{m}$. Heavy solid line: measurements, light solid line: FLEXPART Experiment 1, light dashed line: Experiment 2 (see Table 2).

simulation obtained using an effective dust source now allows us to compare the simulation results to the aircraft observations.

5.1. Comparison to Airborne Dust Size Distributions

The two vertical profiles across the southern edge of the dust plume flown by the BAe-146 during the afternoon of 20 June 2011 along transect AB yielded size-resolved aerosol number concentrations with a high vertical resolution at both locations. The data obtained from a suite of instruments onboard the aircraft (see section 2) have been classified into accumulation (0.1–3 μm), coarse (3–30 μm) and giant mode (30–300 μm) aerosol categories, following *Ryder et al.* [2013b]. Based on the PSD measurements and assuming a density of 2.65 g cm^{-3} for the dust material, vertical profiles of dust mass concentration with a vertical resolution of $\sim 100 \text{ m}$ have been calculated. These measurements will now be used for evaluating the initial aerosol size distribution applied in the FLEXPART dust module.

The measured aerosol mass concentration for the profile A (south of the dust plume) shows that most of the aerosol mass is contained in the coarse mode (Figure 12a, thick red line). However, a substantial contribution to total mass is made by giant mode particles (thick black line), and a lesser contribution by the accumulation mode (thick blue line). Data gaps at some vertical levels and the generally high variability may be due to the small number of giant particles encountered by the aircraft. The vertical mass distributions are fairly homogeneous in the lower 5.0 km msl (the altitudes at 5–6 km have been masked out due to potential cloud influence). Profile B (inside the dust plume) shows higher mass concentrations than profile A (Figure 12b), in particular for the coarse mode (thick red line), but also for the accumulation mode below $\sim 4 \text{ km}$ agl (thick black line). The contribution of coarse particles is similar for both profiles. Above 4 km msl, mass concentrations are markedly lower for the coarse mode at point B, in qualitative agreement with the BAe-146 lidar observations (Figure 7b, see also section 5.4).

Table 2. Sensitivity Experiments Conducted With Different Variations of the Input Parameters^a

Experiment	Duration (h)	Wind Speed (m s^{-1})	Threshold Velocity (m s^{-1})	Total Mass (kg)	Dust Flux ($\text{g m}^{-2} \text{12 h}^{-1}$)
1	12	25	6	3.73E+10	359.1
2	12	20	6	1.76E+10	169.3
3	12	15	6	6.4E+09	61.2

^aAll releases were in the lowermost 4 km and were started from 0000 UTC on 19 June 2011 for the given duration in the dust source region shown in Figure 8b (black line). Experiment 1 is the “best match” case.

When comparing the observations to the model simulations, we focus on the magnitude and general shape of the dust concentration profiles. The model simulation (thin lines in Figure 12) has a smoothed appearance relative to the noisier measurements, which are more strongly affected by local conditions and turbulence. For the accumulation mode and coarse mode categories at profile A, there is reasonable agreement between the aircraft data and the “best match” simulation (Figure 12a, solid thin black and red lines). This points to a realistic initial PSD for these two size categories. The fairly homogeneous vertical structure up to 5 km msl is well captured, as well as the decrease in concentration at higher altitudes, which is mainly a result of the realistically simulated depth of the PBL and the associated vertical mixing of dust. The giant mode category is strongly underestimated and almost absent from the model simulation (thin blue lines). While the measurements show a well-mixed profile for the giant mode, the simulation shows a low-level maximum.

For the profile within the dust plume, the simulation shows general agreement with the aircraft data but clearly misses some of the vertical variability (Figure 12b). In particular, the abrupt change to lower mass concentrations above ~ 3.8 km msl for the accumulation and coarse mode categories is not captured. Again, the giant mode mass contribution is strongly underestimated, by about three orders of magnitude (thin blue line). In addition, the accumulation mode contribution is underestimated by an order of magnitude below 3.8 km msl (thin black line). The more substantial disagreement for profile B may indicate that additional sources and processes contribute to the observed dust profile at that northern location, leading to an enhancement of dust concentrations below ~ 3.8 km msl, such as continuous dust mobilization after 1200 UTC on 19 June 2011 from local dry convection within the daytime CBL. Additionally, further dust sources may have contributed to this profile, containing a higher fraction of accumulation mode particles, for example, suspended within the northeasterly winds from Algeria, directed toward the heat low.

5.2. Sensitivity Experiments

Simulated dust mass concentrations in FLEXPART depend on several parameters. These include the duration of a dust release, the threshold wind velocity, the wind velocity itself, the height of the dust release column, the initial particle size distribution, and the scaling constant C. These parameters, except for the initial PSD, have been varied systematically to test the sensitivity of the FLEXPART dust simulation results. For brevity, only results of the variation of the wind speed are discussed here in detail. The dashed and solid thin lines in Figure 12 show two simulations that bracket the range of observed concentrations, while being based on plausible parameter combinations. Experiment 1 (wind speed of 15 m s^{-1} in the release area) with a dust mass flux of $359.1 \text{ g m}^{-2} \text{12 h}^{-1}$ is shown by the solid lines, whereas Experiment 2 (wind speed of 12 m s^{-1} in the release area) with a dust mass flux of $169.3 \text{ g m}^{-2} \text{12 h}^{-1}$ is indicated by the dashed lines (Table 2). Experiment 1 has a dust mass in the column more than twice as large as in Experiment 2 for both profiles (Table 3). The 12 h emission totals for both simulations have magnitudes similar to other models [e.g., Schepanski *et al.*, 2009]. The atmospheric dust concentration in these emission experiments scales linearly with the surface dust mass flux. The observed variability for each size category matches roughly with the range spanned by the two experiments (Figure 12). The sensitivity to changes in threshold velocity becomes smaller with increasing wind speeds, as the term u^2 in equation (1) will quickly dominate. The underestimated variability of the simulated vertical profiles may to some extent be reproducible by imposing temporal and spatial variability to the emissions in the dust source region.

Table 3. Total Column Dust Load from PSD Instruments and FLEXPART Simulations Named Experiments 1 and 2

Profile	Source	Accumulation Mode (mg m^{-2})	Coarse Mode (mg m^{-2})	Giant Mode (mg m^{-2})
A	Measured	136.7	1908.6	119.2
	Experiment 1	38.4	1791.6	0.075
	Experiment 2	12.6	588.6	0.025
B	Measured	7.3	1194.3	455.6
	Experiment 1	7.4	610.6	0.033
	Experiment 2	2.4	200.7	0.011

The reason for the underestimation of the giant mode size range may be threefold. First, the initial PSD underweights the giant mode category, since it only extends up to $63\ \mu\text{m}$ in the model, whereas the measured PSD reaches $300\ \mu\text{m}$. Second, it is possible that the giant mode particles originate from more recent dust mobilization events, or continued mobilization within the CBL along the transport path, which are not included in the simulation. This is supported by the fact that the most northwesterly (and therefore in nature last activated) grid cell of the manual release field ($4\text{--}5^\circ\text{W}$, $22\text{--}23^\circ\text{N}$) is very important for obtaining the good correspondence between simulation and measurements in Figure 12 at all size categories (not shown). A third possibility is that settling processes in the FLEXPART model overestimate the dry deposition of large particles. A sensitivity run with the same emitted loading but a shorter dust emission period of 1 h instead of 12 h contains hardly any giant mode particles, pointing toward the settling process as an important factor (not shown). This is further confirmed by a sensitivity run with dust emission limited to 0–2 km agl, which almost completely removes the giant mode contributions (not shown). The overly rapid sedimentation of giant particles could also point to a lack of representing the suspension of such particles in the atmosphere due to vertical turbulent kinetic energy [Rosenberg *et al.*, 2014]. Finally, note that the chosen PSD in the FLEXPART simulations only extends up to $63\ \mu\text{m}$ since larger particles almost instantly sediment out of the atmosphere in the model (in contrast to measurements).

Both simulations are run with fairly high sustained wind speeds to obtain a dust concentration in the target area that matches with the observations. These wind speeds may be lowered depending on the exact value of the empirical emission factor C in equation (1). The emission factor C integrates the effect of several parameterized processes as a tuning constant and is therefore model dependent. C has been estimated as $0.7\ \mu\text{g s}^2\ \text{m}^{-5}$ (with a range from 0.4 to $1.2\ \mu\text{g s}^2\ \text{m}^{-5}$) from the global climate model study of Tegen and Fung [1994] but may need to take a different value for the model and PSD applied here. Changing C would affect all particle sizes equally. If a larger fraction of the mass were associated with the giant mode fraction, as suggested by the results above, then the total released mass would have to be spread differently among the size categories by using a different initial PSD, which would require a general increase of dust emission in order to maintain the agreement for the coarse and accumulation mode categories. In the long run, these difficulties call for the use of more sophisticated, direct parameterizations of dust emission based on first principles, such as the dust mobilization scheme proposed by Kok [2011].

5.3. Comparison to Airborne Extinction Measurements

In order to quantitatively compare the FLEXPART data to the previously discussed extinction profiles from the nephelometer and PSAP, lidar, and particle size distribution, the model data are converted to units of extinction, using the same principle as described in section 3.2.2. For point A (Figure 8a), the FLEXPART profile (short dashed line) is on the low end of the range with values of $\sim 1.5 \times 10^{-4}\ \text{m}^{-1}$. This is similar to the estimate from the PSD (long dashed line) and may suggest that the extinction factor $k_{\text{ext}} = 1.22$ is too low for the data at hand. For the profile at point B (Figure 8b), within the dust plume, FLEXPART estimates are $\sim 3 \times 10^{-4}\ \text{m}^{-1}$ (short dashed line), which appears similar compared to the lidar (thick line), biased high compared to the PSD data (long dashed line) and biased low compared to the nephelometer + PSAP data below 3 km asl.

Comparing nephelometer + PSAP extinction and FLEXPART simulated extinction shows that the general dust gradient along transect AB is fairly well reproduced (Figure 8d). An obvious low bias of $3\text{--}5 \times 10^{-4}\ \text{m}^{-1}$, however, is present in the simulation, which increases toward the northern end of the transect. Note that such a bias is well within the range of uncertainty for the parameter k_{ext} , as discussed previously (section 3.2.2).

Together with the disagreement observed between the extinction estimates for the vertical profiles, this may indicate that our approach to convert concentration to extinction may be generally too simplified.

5.4. Comparison With Airborne Lidar Data

Using the best estimate for a dust source strength from the manual inversion procedure obtained here (Experiment 1), we now evaluate how the larger spatial structure of the simulated plume agrees with extinction retrieved from lidar observations.

The extinction along transect AB from the FLEXPART simulation is shown in Figure 7c. The simulation shows a horizontal dust gradient with higher concentrations at the northern end, similar to the lidar data (Figure 7b). In the vertical, the simulated plume does not extend beyond 5 km msl and has less variability at the CBL top, in contrast to the lidar measurements. The residual layers above 5 km msl are not simulated and are thus confirmed to be likely of different age and/or origin than the dust below. Overall, the good qualitative and quantitative comparison increases confidence that the high dust load below 5 km msl was indeed mobilized by the MCS over central Mali 40 h earlier and that the dust transport simulated based on ERA-Interim reanalyses with FLEXPART did work reliably in that aspect.

A similar comparison is now carried out for the eastern transect of the Falcon 20 flight (cf. Figure 4). As shown in Figure 5c, the dust plume is concentrated between 23 and 24.5°N in the model. The southern edge of the simulated dust plume approximately corresponds to a concentration change at the CBL top apparent in Figure 5b, south of 23.2°N. In the simulation, higher concentrations are apparent near the surface than at higher altitudes, in contrast to the BAe-146 transect discussed before. Again, the vertical extent hardly exceeds 5 km msl, in reasonable agreement with the observed lidar transect (Figure 5b). Due to strong extinction, it is not possible to compare the aerosol structure in the lower part of the CBL. An obvious difference between simulation and observations, however, is the modification of the CBL by moist convective processes. The vertical mixing by convection leads to a much more inhomogeneous vertical structure than in the simulations. There appears to be too little moisture in that part of the transect in the ECMWF model to trigger cumulus clouds (Figure 5c, white contours). Parts of the additional moisture may have been supplied by the cold pool outflow and are therefore not present in the analysis data.

6. Discussion

6.1. Potential for Inverse Methods

The procedure leading to the “best match” simulation (section 4.2) can be described as a manual equivalent to commonly used mathematical inversion methods [e.g., *Stohl et al.*, 2009; *Kristiansen et al.*, 2012]. If such a formal, objective inversion method was applied to this case, the available data would leave us with a strongly underconstrained problem, enabling few modifications of the a priori fields. In particular, the considerable spatial heterogeneity of the dust plume and the uncertainty of the winds in the region make it difficult to identify a unique solution with the limited data at hand. We therefore consider the combination of individual dust simulations applied here to obtain the “best match” simulation as a useful alternative to provide an indication where the dust source would need to be located according to the model assuming the transport processes to be reliable. This procedure clearly brings forward the deficiencies of the analysis data with respect to simulating dust emission in the case studied here. While the steps we have taken may appear complex, they are fully generic and can be applied to other regions and data sets. Future campaigns with larger spatial coverage, and more frequent sampling of a dust plume, and/or additional remote sensing products may enable the direct application of mathematical inversion methods. For example, quantitative information of atmospheric dust load from geostationary satellites [e.g., *Gu et al.*, 2003], repeated airborne lidar overpasses, and in situ sampling of a dust plume could be combined to give a more reliable estimate of emission at the dust source.

6.2. Improving Simulated Dust Emission Due To Moist Convection

As evident from this study, dust emission associated with moist convection remains a key obstacle to successfully simulating dust transport and distribution in the Sahara. Dust mobilization by haboobs was responsible for 33–72% of dust load (depending on the haboob definition) at Fennec supersite 1 (BBM) in general [*Cowie et al.*, 2014], as well as during June 2011 and in particular during the period studied here [*Marshall et al.*, 2013; *Allen et al.*, 2013]. In addition, several earlier case studies demonstrated the

substantial potential for dust mobilization from cold pool outflow and density currents [Marsham *et al.*, 2008; Bou Karam *et al.*, 2008, 2014; Kocha *et al.*, 2013]. As long as the horizontal resolution of global models requires the hydrostatic assumption, moist convective processes will need to be parameterized. Global weather prediction models may be run at sufficient resolution in the near future to represent deep convection and convective organization explicitly (some limited-area models already are run operationally at sufficient resolution), but for climate models, the problem will remain for the time being [e.g., Evan *et al.*, 2014] and calls for ways to parameterize dust mobilization from cold pool outflow.

A first improvement to the parameterization of dust mobilization may come from the consideration of wind gustiness as a mobilization parameter [Cakmur *et al.*, 2004; Morcrette *et al.*, 2008]. As has been shown in section 4.1, this can lead to substantial increases in the mobilized dust amount when using a threshold velocity scheme, such as equation (1), and may require retuning using the scaling parameter C . In a model with parameterized convection, however, cold pool-related dust emission may only be improved when moist convection affects wind gusts in a model [e.g., Bechtold and Bilot, 2009]. It is however equally important to form a pressure gradient at the surface driving the spread of the cold pools, as can be seen from the offset between the MCS region and the manually identified dust mobilization regions here (see section 4.2). Pantillon *et al.* [2015] recently made an important step forward by parameterizing the convective cold pool by introducing a radial spreading of the downward mass flux in a convection scheme. Another possibility to address this problem could be to parameterize surface winds with a single-layer cellular automata. Haboob winds could then extend radially from the center of the downdraft trigger region and could be kept separate from the wind speed at the model grid scale. Such an approach has been proposed by Grandpeix and Lafore [2010], where circular spreading cold pools triggered by convective downdrafts are introduced at the subgrid-scale in a global model. Cellular automata with a simple updating principle have been shown to provide realistic results with respect to the role of cold pools in organizing deep convection [Bengtsson *et al.*, 2013] but so far have not been exploited to the benefit of improving dust mobilization.

If such a cold pool parameterization was developed and implemented into a model code and run online, dust emission could be triggered as haboobs advance at the model time step. While such an online approach is possible in a Eulerian framework, typical Lagrangian simulations run off-line based on model output at a given time interval (here 3 h). One solution could be to provide the time-integrated dust uplift potential as a model output field, which can then be used for dust emission in off-line models. Further improvement for Lagrangian off-line simulations may come from the more frequent supply of model winds in pace with resolution increments, from the use of time-averaged wind speed output, and from taking into account the variance of the winds [Bowman *et al.*, 2013].

7. Summary and Conclusions

In this study, we use the multifaceted and comprehensive field data acquired during the Fennec/LADUNEX campaign in the western Sahara during June 2011 to investigate the main factors determining the success or failure of dust plume simulation with the Lagrangian particle transport model FLEXPART. A case study focuses on the evolution of a large haboob, a dust plume caused by cold pools associated with organized deep convection. It is shown that by using high-resolution meteorological analyses from the ECMWF the dust transport model can provide a realistic evolution of a dust plume over a 40 h simulation period. A crucial prerequisite for such a simulation is however that dust mobilization be suitably specified.

Due to deficiencies in the meteorological analyses and the treatment of moist convection in parameterizations, no MCS is present in the analysis data, and no cold pools emerge. Direct calculation of dust mobilization based on wind speed and wind gusts remains unsuccessful. Therefore, dust emission from the MCS has to be manually specified in what is an effective dust source region into which the haboob has expanded 6 h after being triggered by moist convection, according to satellite data. Apart from the missing cold pools, the mesoscale winds in the region were well represented in the analysis data, as evidenced by the realistic shape of the dust plume simulated with FLEXPART, allowing us to test the influence of different parameters on dust transport during this case.

In general, providing a unique fit of the model results to observational data is difficult, if not impossible, due to several poorly constrained parameters when calculating dust emission from a threshold parameterization.

Mathematical inversion methods cannot be used with our current setup, as they are underconstrained and thus render the problem ill-posed. The manual inversion applied here, however, can serve as a blueprint for future, more objective inversion studies.

The comprehensive in situ and remote sensing aircraft measurements across part of the dust plume show that particle size distributions are realistically simulated for the accumulation and coarse mode but strongly underestimate the contribution of giant particles, despite the model size distribution extending to 63 μm , considerably higher than typically considered in dust models. This may be partly due to the underestimation of continuous mobilization but also points to more fundamental problems related to the inclusion and treatment of giant particles during atmospheric transport. The validation of model simulations using extinction measurements is affected by considerable uncertainty in calculating extinction values from dust concentration. Using dust mobilization schemes that are more directly based on physical principles may be a way forward to reduce the uncertainty in the emitted dust PSD.

The main conclusion from this work is that simulating dust emission is a major limiting factor for obtaining realistic dust simulations in the summertime Sahara, not only for grid-scale models but also for Lagrangian models. The primary reason here is that parameterized moist convection does not match with observations, and no cold pools are formed. A logical next step to improve the present results could be to repeat the present analysis with a meteorological model simulation that explicitly resolves moist convection, thereby further underscoring the immense value of the Fennec/LADUNEX measurements as a new key data set for dust model validation.

Acknowledgments

EUFAR is acknowledged for funding the Transnational Access grant LADUNEX. T.M.L. acknowledges EUFAR for funding through an Education and Training activity. Fennec was funded by a NERC consortium grant (NE/G017166/1). Airborne data were obtained using the BAe-146-301 Atmospheric Research Aircraft (ARA) flown by Directflight Ltd. and managed by the Facility for Airborne Atmospheric Measurements (FAAM), which is a joint entity of the Natural Environment Research Council (NERC) and the Met Office. P.K. acknowledges funding from ERC grant 257543 Desert Storms. The Fennec-France project is funded by the Agence Nationale de la Recherche (ANR), the Institut National des Sciences de l'Univers (INSU/CNRS) through the LEFE program, by the Centre National d'Etudes Spatiales (CNES) through the TOSCA program and by Météo-France. Many thanks to the SAFIRE team for the dropsonde data from the Falcon 20 as well as to J. Pelon (LATMOS). The authors are grateful to D. Bruneau and P. Genau (LATMOS), F. Blouzon, and A. Abchiche (DT/INSU) for operating the LNG system in the Falcon 20. We also thank Eumetsat for providing the "dust RGB" product. MeteoSwiss is acknowledged for provision of ECMWF analysis data. Dave Winker is acknowledged for providing rapid access to the CALIOP lidar data during the campaign. John Marsham is thanked for constructive feedback on an earlier version of this manuscript. Heini Wernli, Andreas Stohl, and Massimo Cassiani are thanked for valuable input during different stages of this research. We thank three anonymous reviewers for their comments, which helped to significantly improve the manuscript. Data used to produce the results of this paper and software code are available on request from the corresponding author at harald.sodemann@uib.no.

References

- Albani, S., N. M. Mahowald, A. T. Perry, R. A. Scanza, C. S. Zender, N. G. Heavens, V. Maggi, J. F. Kok, and B. L. Otto Bliesner (2014), Improved dust representation in the community atmosphere model, *J. Adv. Model. Earth Syst.*, doi:10.1002/2013MS000279.
- Allen, C. J. T., R. Washington, and S. Engelstaedter (2013), Dust emission and transport mechanisms in the central Sahara: Fennec ground-based observations from Bordj Badji Mokhtar, June 2011, *J. Geophys. Res. Atmos.*, *118*, 6212–6232, doi:10.1002/jgrd.50534.
- Ansmann, A., A. Petzold, K. Kandler, and I. Tegen (2011), Saharan Mineral Dust Experiments SAMUM-1 and SAMUM-2: What have we learned?, *Tellus B*, doi:10.1111/j.1600-0889.2011.00555.x.
- Ashpole, I., and R. Washington (2013), A new high-resolution central and western Saharan summertime dust source map from automated satellite dust plume tracking, *J. Geophys. Res. Atmos.*, *118*, 6981–6995, doi:10.1002/jgrd.50554.
- Banks, J. R., H. E. Brindley, C. Flamant, M. J. Garay, N. C. Hsu, O. V. Kalashnikova, L. Klüser, and A. M. Sayer (2013), Intercomparison of satellite dust retrieval products over the West African Sahara during the Fennec campaign in June 2011, *Remote Sens. Environ.*, *136*, 99–116, doi:10.1016/j.rse.2013.05.003.
- Bechtold, P., and J.-R. Bidlot (2009), Parametrization of convective gusts, *ECMWF Newsl.*, *119*, 15–18.
- Bengtsson, L., M. Steinheimer, P. Bechtold, and J.-F. Geleyn (2013), A stochastic parametrization for deep convection using cellular automata, *Q. J. R. Meteorol. Soc.*, *139*(675), 1533–1543, doi:10.1002/qj.2108.
- Berry, G. J., and C. Thorncroft (2005), Case study of an intense African easterly wave, *Mon. Weather Rev.*, *133*(4), 752–766.
- Bodhaine, B. A., N. B. Wood, E. G. Dutton, and J. R. Slusser (1999), On Rayleigh optical depth calculations, *J. Atmos. Oceanic Technol.*, *16*(11), 1854–1861.
- Bou Karam, D., C. Flamant, P. Knippertz, O. Reitebuch, J. Pelon, M. Chong, and A. Dabas (2008), Dust emissions over the Sahel associated with the West African monsoon intertropical discontinuity region: A representative case-study, *Q. J. R. Meteorol. Soc.*, *134*(632), 621–634, doi:10.1002/qj.244.
- Bou Karam, D., E. Williams, M. Janiga, C. Flamant, M. McGraw, J. Cuesta, A. Auby, and C. Thorncroft (2014), Synoptic-scale dust emissions over the Sahara desert initiated by a moist convective cold pool in early August 2006, *Q. J. R. Meteorol. Soc.*, doi:10.1002/qj.2326.
- Bowman, K. P., J. C. Lin, A. Stohl, R. Draxler, P. Konopka, A. Andrews, and D. Brunner (2013), Input data requirements for Lagrangian trajectory models, *Bull. Am. Meteorol. Soc.*, *94*(7), 1051–1058, doi:10.1175/BAMS-D-12-00076.1.
- Braun, S. A., J. A. Sippel, C.-L. Shie, and R. A. Boller (2013), The evolution and role of the Saharan air layer during Hurricane Helene (2006), *Mon. Weather Rev.*, *141*(12), doi:10.1175/MWR-D-13-00045.1.
- Brindley, H., P. Knippertz, C. Ryder, and I. Ashpole (2012), A critical evaluation of the ability of the Spinning Enhanced Visible and Infrared Imager (SEVIRI) thermal infrared red-green-blue rendering to identify dust events: Theoretical analysis, *J. Geophys. Res.*, *117*, D07201, doi:10.1029/2011JD017326.
- Cakmur, R. V., R. L. Miller, and O. Torres (2004), Incorporating the effect of small-scale circulations upon dust emission in an atmospheric general circulation model, *J. Geophys. Res.*, *109*, D07201, doi:10.1029/2003JD004067.
- Chomette, O., M. Legrand, and B. Marticorena (1999), Determination of the wind speed threshold for the emission of desert dust using satellite remote sensing in the thermal infrared, *J. Geophys. Res.*, *104*, 31,207–31,215, doi:10.1029/1999JD000756.
- Couvreux, F., F. Guichard, and O. Bock (2010), Synoptic variability of the monsoon flux over West Africa prior to the onset, *QJRMSS*, *136*(s1), 159–173, doi:10.1002/qj.473.
- Cowie, S. M., P. Knippertz, and J. H. Marsham (2014), A climatology of dust emission events from Northern Africa using long-term surface observations, *Atmos. Chem. Phys.*, *14*, 8579–8597, doi:10.5194/acp-14-8579-2014.
- Cuesta, J., et al. (2008), Multiplatform observations of the seasonal evolution of the Saharan atmospheric boundary layer in Tamanrasset, Algeria, in the framework of the African monsoon multidisciplinary analysis field campaign conducted in 2006, *J. Geophys. Res.*, *113*, D00C07, doi:10.1029/2007JD009417.
- Cuesta, J., J. H. Marsham, D. J. Parker, and C. Flamant (2009), Dynamical mechanisms controlling the vertical redistribution of dust and the thermodynamic structure of the West Saharan atmospheric boundary layer during summer, *Atmos. Sci. Lett.*, *10*(1), 34–42, doi:10.1002/asl.207.

- d'Almeida, G. A., and L. Schütz (1983), Number, mass and volume distributions of mineral aerosol and soils of the Sahara, *J. Climate Appl. Meteorol.*, *22*(2), 233–243.
- de Villiers, R. A., G. Ancellet, J. Pelon, B. Quennehen, A. Schwarzenboeck, J. F. Gayet, and K. S. Law (2010), Airborne measurements of aerosol optical properties related to early spring transport of mid-latitude sources into the arctic, *Atmos. Chem. Phys.*, *10*(11), 5011–5030, doi:10.5194/acp-10-5011-2010.
- Draxler, R. R., and G. D. Hess (1998), An overview of the HYSPLIT_4 modelling system for trajectories, dispersion, and deposition, *Aust. Meteorol. Mag.*, *47*, 295–308.
- Draxler, R. R., D. A. Gillette, J. S. Kirkpatrick, and J. Heller (2001), Estimating PM10 air concentrations from dust storms in Iraq, Kuwait and Saudi Arabia, *Atmos. Environ.*, *35*(25), 4315–4330, doi:10.1016/S1352-2310(01)00159-5.
- Draxler, R. R., P. Ginoux, and A. F. Stein (2010), An empirically derived emission algorithm for wind-blown dust, *J. Geophys. Res.*, *115*, D16212, doi:10.1029/2009JD013167.
- Duce, R. A., et al. (1991), The atmospheric input of trace gas species to the world ocean, *Global Biogeochem. Cycles*, *5*, 193–259, doi:10.1029/91GB01778.
- Dunion, J. P., and C. S. Velden (2004), The impact of the Saharan air layer on Atlantic tropical cyclone activity, *Bull. Am. Meteorol. Soc.*, *85*(3), 353–365, doi:10.1175/BAMS-85-3-353.
- Eckhardt, S., A. J. Prata, P. Seibert, K. Stebel, and A. Stohl (2008), Estimation of the vertical profile of sulfur dioxide injection into the atmosphere by a volcanic eruption using satellite column measurements and inverse transport modeling, *Atmos. Chem. Phys.*, *8*, 3881–3897.
- Emanuel, K. A., and M. Živković-Rothman (1999), Development and evaluation of a convection scheme for use in climate models, *J. Atmos. Sci.*, *56*, 1766–1782.
- Emmel, C., P. Knippertz, and O. Schulz (2010), Climatology of convective density currents in the southern foothills of the Atlas Mountains, *J. Geophys. Res.*, *115*, D11115, doi:10.1029/2009JD012863.
- Evan, A. T., C. Flamant, S. Fiedler, and O. Doherty (2014), An analysis of aeolian dust in climate models, *Geophys. Res. Lett.*, *41*, 5996–6001, doi:10.1002/2014GL060545.
- Fernald, F. G., B. M. Herman, and J. A. Reagan (1972), Determination of aerosol height distributions by lidar, *J. Appl. Meteorol.*, *11*(April), 482–489, doi:10.1175/1520-0450(1972)011<0482:DOAHDB>2.0.CO;2.
- Flamant, C., J. P. Chaboureau, D. J. Parker, C. M. Taylor, J. P. Cammas, O. Bock, F. Timouk, and J. Pelon (2007), Airborne observations of the impact of a convective system on the planetary boundary layer thermodynamics and aerosol distribution in the inter-tropical discontinuity region of the West African monsoon, *Q. J. R. Meteorol. Soc.*, *133*(626), 1175–1189, doi:10.1002/qj.97.
- Flamant, C., C. Lavaysse, M. C. Todd, J. P. Chaboureau, and J. Pelon (2009a), Multi-platform observations of a springtime case of Bodélé and Sudan dust emission, transport and scavenging over West Africa, *Q. J. R. Meteorol. Soc.*, *135*(639), 413–430, doi:10.1002/qj.376.
- Flamant, C., P. Knippertz, D. J. Parker, J. P. Chaboureau, C. Lavaysse, A. Agusti-Panareda, and L. Kergoat (2009b), The impact of a mesoscale convective system cold pool on the northward propagation of the intertropical discontinuity over West Africa, *Q. J. R. Meteorol. Soc.*, *135*(638), 139–159, doi:10.1002/qj.357.
- Foret, G., G. Bergametti, F. Dulac, and L. Menut (2006), An optimized particle size bin scheme for modeling mineral dust aerosol, *J. Geophys. Res.*, *111*, D17310, doi:10.1029/2005JD006797.
- García-Carreras, L., J. H. Marsham, D. J. Parker, C. L. Bain, S. Milton, A. Saci, M. Salah-Ferroudj, B. Ouchene, and R. Washington (2013), The impact of convective cold pool outflows on model biases in the Sahara, *Geophys. Res. Lett.*, *40*, 1647–1652, doi:10.1002/grl.50239.
- Goudie, A. S., and N. J. Middleton (2001), Saharan dust storms: Nature and consequences, *Earth Sci. Rev.*, *56*, 179–204.
- Grandpeix, J.-Y., and J.-P. Lafore (2010), A density current parameterization coupled with Emanuel's convection scheme. Part I: The Models, *J. Atmos. Sci.*, *67*(4), 881–897, doi:10.1175/2009JAS3044.1.
- Gu, Y. X., W. I. Rose, and G. J. S. Bluth (2003), Retrieval of mass and sizes of particles in sandstorms using two MODIS IR bands: A case study of April 7, 2001 sandstorm in China, *Geophys. Res. Lett.*, *30*(15), 1805, doi:10.1029/2003GL017405.
- Hall, N. M. J., G. N. Kiladis, and C. D. Thorncroft (2006), Three-Dimensional Structure and Dynamics of African Easterly Waves. Part II: Dynamical Modes, *J. Atmos. Sci.*, *63*, 2231–2245, doi:10.1175/JAS3742.1.
- Hänel, G. (1976), The properties of atmospheric aerosol particles as functions of relative humidity at thermodynamic equilibrium with surrounding moist air, *Adv. Geophys.*, *19*, 73–188.
- Haywood, J. M., et al. (2008), Overview of the dust and biomass-burning experiment and African monsoon multidisciplinary analysis special observing period-0, *J. Geophys. Res.*, *113*, D00C17, doi:10.1029/2008JD010077.
- Heinold, B., J. Helmert, O. Hellmuth, R. Wolke, A. Ansmann, B. Martcorena, B. Laurent, and I. Tegen (2007), Regional modeling of Saharan dust events using LM-MUSCAT: Model description and case studies, *J. Geophys. Res.*, *112*, D11204, doi:10.1029/2006JD007443.
- Heinold, B., P. Knippertz, J. H. Marsham, S. Fiedler, N. S. Dixon, K. Schepanski, B. Laurent, and I. Tegen (2013), The role of deep convection and nocturnal low-level jets for dust emission in summertime West Africa: Estimates from convection-permitting simulations, *J. Geophys. Res. Atmos.*, *118*, 4385–4400, doi:10.1002/jgrd.50402.
- Heintzenberg, J. (2009), The SAMUM-1 experiment over Southern Morocco: Overview and introduction, *Tellus*, *61*, 2–11.
- Hertel, O., J. Christensen, E. H. Runge, W. A. H. Asman, R. Berkowicz, M. F. Hovmand, and Ø. Hov (1995), Development and testing of a new variable scale air-pollution model—ACDEP, *Atmos. Environ.*, *29*(11), 1267–1290.
- Hobby, M., et al. (2013), The Fennec automatic weather station (AWS) network: Monitoring the Saharan climate system, *J. Atmos. Oceanic Technol.*, *30*(4), 709–724, doi:10.1175/JTECH-D-12-00037.1.
- Huneus, N., et al. (2011), Global dust model intercomparison in AeroCom phase I, *Atmos. Chem. Phys.*, *11*(15), 7781–7816, doi:10.5194/acp-11-7781-2011.
- Johnson, B. T., and S. R. Osborne (2011), Physical and optical properties of mineral dust aerosol measured by aircraft during the GERBILS campaign, *Q. J. R. Meteorol. Soc.*, *137*(658), 1117–1130, doi:10.1002/qj.777.
- Klein, H., S. Nickovic, W. Haunold, U. Bundke, B. Nillius, M. Ebert, S. Weinbruch, L. Schuetz, Z. Levin, and L. A. Barrie (2010), Saharan dust and ice nuclei over central Europe, *Atmos. Chem. Phys.*, *10*(21), 10,211–10,221.
- Knippertz, P. (2008), Dust emissions in the West African heat trough—The role of the diurnal cycle and of extratropical disturbances, *Meteorol. Z.*, *17*(5), 553–563, doi:10.1127/0941-2948/2008/0315.
- Knippertz, P., and M. C. Todd (2010), The central west Saharan dust hot spot and its relation to African easterly waves and extratropical disturbances, *J. Geophys. Res.*, *115*, D12117, doi:10.1029/2009JD012819.
- Knippertz, P., and M. C. Todd (2012), Mineral dust aerosols over the Sahara: Meteorological controls on emission and transport and implications for modeling, *Rev. Geophys.*, *50*, 1–28, doi:10.1029/2011RG000362.
- Knippertz, P., C. Deutscher, K. Kandler, T. Müller, O. Schulz, and L. Schütz (2007), Dust mobilization due to density currents in the Atlas region: Observations from the Saharan Mineral Dust Experiment 2006 field campaign, *J. Geophys. Res.*, *112*, D21109, doi:10.1029/2007JD008774.

- Knippertz, P., J. Trentmann, and A. Seifert (2009), High-resolution simulations of convective cold pools over the northwestern Sahara, *J. Geophys. Res.*, *114*, D08110, doi:10.1029/2008JD011271.
- Kocha, C., P. Tulet, J. P. Lafore, and C. Flamant (2013), The importance of the diurnal cycle of aerosol optical depth in West Africa, *Geophys. Res. Lett.*, *40*, 785–790, doi:10.1002/grl.50143.
- Kok, J. F. (2011), A scaling theory for the size distribution of emitted dust aerosols suggests climate models underestimate the size of the global dust cycle, *Proc. Natl. Acad. Sci. U.S.A.*, *108*(3), 1016–1021.
- Kok, J. F., and N. O. Renno (2009), A comprehensive numerical model of steady state saltation (COMSALT), *J. Geophys. Res.*, *114*, D17204, doi:10.1029/2009JD011702.
- Kristiansen, N. I., et al. (2012), Performance assessment of a volcanic ash transport model mini-ensemble used for inverse modeling of the 2010 Eyjafjallajökull eruption, *J. Geophys. Res.*, *117*, D00U11, doi:10.1029/2011JD016844.
- Lafore, J. P., C. Flamant, and F. Guichard (2011), Progress in understanding of weather systems in West Africa, *Atmos. Sci. Lett.*, *12*, 7–12.
- Lavaysse, C., C. Flamant, S. Janicot, D. J. Parker, J. P. Lafore, B. Sultan, and J. Pelon (2009), Seasonal evolution of the West African heat low: A climatological perspective, *Clim. Dyn.*, *33*(2–3), 313–330, doi:10.1007/s00382-009-0553-4.
- Marengo, F. (2013), Nadir airborne lidar observations of deep aerosol layers, *Atmos. Meas. Tech.*, *6*, 2055–2064.
- Marengo, F., B. Johnson, K. Turnbull, S. Newman, J. Haywood, H. Webster, and H. Ricketts (2011), Airborne lidar observations of the 2010 Eyjafjallajökull volcanic ash plume, *J. Geophys. Res.*, *116*, D00U05, doi:10.1029/2011JD016396.
- Marsham, J. H., D. J. Parker, C. M. Grams, C. M. Taylor, and J. M. Haywood (2008), Uplift of Saharan dust south of the intertropical discontinuity, *J. Geophys. Res.*, *113*, D21102, doi:10.1029/2008JD009844.
- Marsham, J. H., P. Knippertz, N. S. Dixon, D. J. Parker, and G. M. S. Lister (2011), The importance of the representation of deep convection for modeled dust-generating winds over West Africa during summer, *Geophys. Res. Lett.*, *38*, L16803, doi:10.1029/2011GL048368.
- Marsham, J. H., et al. (2013), Meteorology and dust in the central Sahara: Observations from Fennec supersite-1 during the June 2011 intensive observation period, *J. Geophys. Res. Atmos.*, *118*, 4069–4089, doi:10.1002/jgrd.50211.
- Marticorena, B., and G. Bergametti (1995), Modeling the atmospheric dust cycle: 1. Design of a soil derived dust emission scheme, *J. Geophys. Res.*, *100*(D8), 16,415–16,430, doi:10.1029/95JD00690.
- Marticorena, B., B. Chatenet, J. L. Rajot, S. Traore, M. Coulibaly, A. Diallo, I. Kone, A. Maman, T. N. Diaye, and A. Zakou (2010), Temporal variability of mineral dust concentrations over West Africa: Analyses of a pluriannual monitoring from the AMMA Sahelian dust transect, *Atmos. Chem. Phys.*, *10*(18), 8899–8915, doi:10.5194/acp-10-8899-2010.
- McConnell, C. L., E. J. Highwood, H. Coe, P. Formenti, B. Anderson, S. Osborne, S. Nava, K. Desboeufs, G. Chen, and M. A. J. Harrison (2008), Seasonal variations of the physical and optical characteristics of Saharan dust: Results from the dust outflow and deposition to the ocean (DODO) experiment, *J. Geophys. Res.*, *113*, D14S05, doi:10.1029/2007JD009606.
- Messenger, C., D. J. Parker, O. Reitebuch, A. Agusti-Panareda, C. M. Taylor, and J. Cuesta (2009), Structure and dynamics of the Saharan atmospheric boundary layer during the West African monsoon onset: Observations and analyses from the research flights of 14 and 17 July 2006, *Q. J. R. Meteorol. Soc.*, *136*(S1), 107–124, doi:10.1002/qj.469.
- Morcrette, J.-J., A. Beljaars, A. Benedetti, L. Jones, and O. Boucher (2008), Sea-salt and dust aerosols in the ECMWF IFS model, *Geophys. Res. Lett.*, *35*, L24813, doi:10.1029/2008GL036041.
- Pantillon, F., P. Knippertz, J. Marsham, and C. Birch (2015), A parameterization of convective dust storms for models with mass-flux convection schemes, *J. Atmos. Sci.*, doi:10.1175/JAS-D-14-0341.1, in press.
- Parker, D. J., C. D. Thorncroft, R. R. Burton, and A. Diongue-Niang (2005a), Analysis of the African easterly jet, using aircraft observations from the JET2000 experiment, *Q. J. R. Meteorol. Soc.*, *131*(608B), 1461–1482.
- Parker, D. J., R. R. Burton, A. Diongue-Niang, R. J. Ellis, M. Felton, C. M. Taylor, C. D. Thorncroft, P. Bessemoulin, and A. M. Tompkins (2005b), The diurnal cycle of the West African monsoon circulation, *Q. J. R. Meteorol. Soc.*, *131*(611), 2839–2860, doi:10.1256/qj.04.52.
- Prospero, J. M., and P. J. Lamb (2003), African droughts and dust transport to the Caribbean: Climate change implications, *Science*, *302*, 1024–1027.
- Rastigejev, Y., R. Park, M. Brenner, and D. Jacob (2010), Resolving intercontinental pollution plumes in global models of atmospheric transport, *J. Geophys. Res.*, *115*, D02302, doi:10.1029/2009JD012568.
- Redelsperger, J. L., C. Thorncroft, A. Diedhiou, T. Lebel, D. Parker, and J. Polcher (2006), African Monsoon Multidisciplinary Analysis: An international project and field campaign, *Bull. Am. Meteorol. Soc.*, *87*(12), 1739–1746, doi:10.1175/BAMS-87-12-1739.
- Roberts, A. J., and P. Knippertz (2014), The formation of a large summertime Saharan dust plume: Convective and synoptic-scale analysis, *J. Geophys. Res. Atmos.*, *119*, 1766–1785, doi:10.1002/(ISSN)2169-8996.
- Rosenberg, P. D., A. R. Dean, P. I. Williams, J. R. Dorsey, A. Minikin, M. A. Pickering, and A. Petzold (2012), Particle sizing calibration with refractive index correction for light scattering optical particle counters and impacts upon PCASP and CDP data collected during the Fennec campaign, *Atmos. Meas. Tech.*, *5*(5), 1147–1163, doi:10.5194/amt-5-1147-2012.
- Rosenberg, P. D., et al. (2014), Quantifying particle size and turbulent scale dependence of dust flux in the Sahara using aircraft measurements, *J. Geophys. Res. Atmos.*, *119*, 7577–7598, doi:10.1002/2013JD021255.
- Ryder, C. L., et al. (2013a), Optical properties of Saharan dust aerosol and contribution from the coarse mode as measured during the Fennec 2011 aircraft campaign, *Atmos. Chem. Phys.*, *13*(1), 303–325, doi:10.5194/acp-13-303-2013.
- Ryder, C. L., E. J. Highwood, T. M. Lai, H. Sodemann, and J. H. Marsham (2013b), Impact of atmospheric transport on the evolution of microphysical and optical properties of Saharan dust, *Geophys. Res. Lett.*, *40*, 2433–2438, doi:10.1002/grl.50482.
- Ryder, C. L., et al. (2015), Advances in understanding mineral dust and boundary layer processes over the Sahara from Fennec aircraft observations, *Atmos. Chem. Phys. Discuss.*, *15*(1), 199–290, doi:10.5194/acpd-15-199-2015.
- Schepanski, K., I. Tegen, M. C. Todd, B. Heinold, G. Bönisch, B. Laurent, and A. Macke (2009), Meteorological processes forcing Saharan dust emission inferred from MSG-SEVIRI observations of subdaily dust source activation and numerical models, *J. Geophys. Res.*, *114*, D10201, doi:10.1029/2008JD010325.
- Shao, Y., M. R. Raupach, and P. A. Findlater (1993), Effect of saltation bombardment on the entrainment of dust by wind, *J. Geophys. Res.*, *98*(D7), 12,719–12,726, doi:10.1029/93JD00396.
- Slinn, W. G. N. (1982), Predictions for particle deposition to vegetative canopies, *Atmos. Environ.*, *16*(7), 1785–1794, doi:10.1016/0004-6981(82)90271-2.
- Sodemann, H., A. Palmer, C. Schwierz, M. Schwikowski, and H. Wernli (2006), The transport history of two Saharan dust events archived in an alpine ice core, *Atmos. Chem. Phys.*, *6*, 667–688.
- Sodemann, H., et al. (2011), Episodes of cross-polar transport in the arctic troposphere during July 2008 as seen from models, satellite, and aircraft observations, *Atmos. Chem. Phys.*, *11*, 3631, doi:10.5194/acp-11-3631-2011.
- Solomos, S., G. Kallos, E. Mavromatidis, and J. Kushnir (2012), Density currents as a desert dust mobilization mechanism, *Atmos. Chem. Phys.*, *12*, 11,199–11,211.

- Stohl, A., C. Forster, A. Frank, P. Seibert, and G. Wotawa (2005), Technical note: The Lagrangian particle dispersion model FLEXPART version 6.2, *Atmos. Chem. Phys.*, *5*, 2461–2474, SRef-ID: 1680-7324/acp/2005-5-2461.
- Stohl, A., et al. (2009), An analytical inversion method for determining regional and global emissions of greenhouse gases: Sensitivity studies and application to halocarbons, *Atmos. Chem. Phys.*, *9*(5), 1597–1620.
- Tegen, I., and I. Fung (1994), Modeling of mineral dust in the atmosphere: Sources, transport, and optical thickness, *J. Geophys. Res.*, *99*(D11), 22,897–22,914, doi:10.1029/94JD01928.
- Tegen, I., S. P. Harrison, K. Kohfeld, I. C. Prentice, M. Coe, and M. Heimann (2002), Impact of vegetation and preferential source areas on global dust aerosol: Results from a model study, *J. Geophys. Res.*, *107*(D21), 4576, doi:10.1029/2001JD000963.
- Thomson, D. J. (1987), Criteria for the selection of stochastic models of particle trajectories in turbulent flows, *J. Fluid Mech.*, *180*, 529–556, doi:10.1017/S0022112087001940.
- Todd, M. C., et al. (2013), Meteorological and dust aerosol conditions over the western Saharan region observed at Fennec supersite 2 during the intensive observation period in June 2011, *J. Geophys. Res. Atmos.*, *118*, 8426–8447, doi:10.1002/jgrd.50470.
- Tompkins, A. M., C. Cardinali, J.-J. Morcrette, and M. Rodwell (2005), Influence of aerosol climatology on forecasts of the African easterly jet, *Geophys. Res. Lett.*, *32*, L10801, doi:10.1029/2004GL022189.
- Washington, R., et al. (2012), Fennec—The Saharan Climate System, *CLIVAR Exch.*, *17*(3), 31–33.
- Weisman, M. L., W. C. Skamarock, and J. B. Klemp (1997), The resolution dependence of explicitly modelled convective systems, *Mon. Weather Rev.*, *125*, 527–548, doi:10.1175/1520-0493(1997)125<0527:TRDOEM>2.0.CO;2.